ELSEVIER

Contents lists available at ScienceDirect

Cold Regions Science and Technology

journal homepage: www.elsevier.com/locate/coldregions





Relating storm-snow avalanche instabilities to data collected from the Differential Emissivity Imaging Disdrometer (DEID)

Travis J. Morrison ^{a,b}, Trent Meisenheimer ^b, Timothy Garrett ^c, Dhiraj Singh ^b, Spencer Donovan ^b, Eric Pardyjak ^{b,*}

- ^a Particle Flux Analytics, Inc., 6300 Sagewood Drive Suite H #623, Park City, 84098, UT, United States
- b University of Utah, Department of Mechanical Engineering, 1495 E 100 S (1550 MEK), Salt Lake City, 84115, UT, United States

ABSTRACT

^c University of Utah, Department of Atmospheric Sciences, 135 S 1460 E (819 WBB), Salt Lake City, 84115, UT, United States

ARTICLE INFO

Keywords: SNOSS model Storm-snow instability DEID Snow-density measurement

. . . .

Storm-snow avalanches are challenging to forecast due to complex alpine terrain and during rapidly changing weather conditions. They can result in loss of lives and significant economic impact. We describe how a new device that continuously measures with high-frequency snowflake mass, size, density, and type, the Differential Emissivity Imaging Disdrometer (DEID), and show how the DEID can be used to aid avalanche forecasting when coupled with a storm-snow stability model. DEID measurements of snow accumulation, snow water equivalent (SWE), and snow density obtained during seventeen storms taken at the mid-Collins Snow-Study Plot at Alta Ski Area in Utah's Central Wasatch mountain range during winter 2020-2021 show excellent agreement with infrequent manual measurements. Additionally, two new variables, the Shape Density Index (SDI) and Complexity, are proposed and used to classify snowflake habit and estimate storm-snow shear strength. We illustrate how these DEID-derived data can be used to identify layers of concern in the storm snow such as density inversions, in real-time without digging snow pits. Furthermore, the DEID-data are used to run four variations of the SNOw Slope Stability model (SNOSS) for the storms investigated. The results are evaluated with data collected from tilt-board tests, infrasound measurements, and visual observations of avalanches. For a total fourteen storms analyzed, the DEID-driven SNOSS-modeled minimum stability index predicts the general stability of the storm-snow as indicated by observed avalanches, both natural and of unknown cause. The results provide a promising approach for nowcasting instabilities within storm-snow layers with a single instrument.

1. Introduction

Storm-snow avalanches arise due to instabilities within the storm-snow layer or at the old-snow/storm-snow interface (American Avalanche Association, 2022). These avalanches often occur in alpine terrain and are the cause of significant hazards to roadways, motorists, maintenance personnel, and infrastructure, closing mountain corridors throughout many areas including Europe, North and South America, and New Zealand. Key ingredients that can lead to avalanches occurring within the storm snow are density inversions (i.e., relatively high-density snow above low-density snow, often refereed to as upside-down snow) and high snow water equivalent (SWE) rates, which increase the overburden stress on storm snow prior to densification due to compactive and metamorphic stresses, which in turn increases the strength of the storm snow below (American Avalanche Association,

2022; Jamieson, 1995). Note that for the scope of this work, the term storm-snow avalanche is utilized rather than storm slab, since the cohesiveness of the slab within the storm-snow layer is not determined, however the depth and density of the potential slab is examined. Due to the subtleties of density variation or snow habit changes within the storm snow and the rapid variability of SWE rate during storms (Singh et al., 2021) forecasting these avalanches with a high degree of spatial and temporal accuracy (sub 1 km and 1 h) has plagued avalanche forecasters and mitigation specialists for decades.

Each year avalanches result in loss of life with significant economic impact. In Europe, on average 100 persons lose their lives to avalanches annually. In North America over the last ten years the Colorado Avalanche Information Center (CAIC) reports that this average has risen to 27 fatalities from avalanches (CAIC, 2022; EAWS, 2022). Monetary costs from damages to infrastructure and road closures as a result of

E-mail address: pardyjak@eng.utah.edu (E. Pardyjak).

^{*} Corresponding author.

avalanches can also cause major problems for local economies. Economic impacts can be difficult to assess, although 30 years ago Voight and Coauthors (1990) estimated that property damages, rescues and snow removal had impacts to the US economy in the millions of dollars. 2014 Icelandic estimates accounting for indirect economic loss along with loss of life find that each fatality in their country may be equal to 1.2 million US dollars (Jóhannesson and Porsteinn, 1992).

This study is focused on highway SR-210, located in Little Cottonwood Canyon (LCC), Utah, United States, which is a high-traffic mountain highway. As a result of storms and mitigation work, LCC closes, on average, 10.4 times for a total 57.3 h per year. On snow years that significantly exceed average accumulations, those numbers can more than double. The cost of such closures has been estimated at over \$2.5 million per day, or \$106,000 per hour in 2019 dollars (Nalli, 2019).

Currently, storm-slab avalanche forecasting requires in-situ observations and weather-forecasting products, specifically, accurate observations of snow density, snow water equivalent (SWE), and precipitation intensity. Even with these data at limited points in space, forecasting storm-slab avalanches presents a challenge due to the highly spatiotemporally varying character of these data and the shear number of variables associated with storm-slab avalanches. The dynamic nature of atmosphere-snow interactions presents an ever complex forecasting problem from a research and practitioner standpoint. Depending on the region and available observing infrastructure, a variety of techniques are used to collect the aforementioned variables. Most commonly, snow scales are combined with acoustic snow depth sensors to measure storm snow density. However this technique only provides very coarse estimates of total storm water content and density. Operational centers can sometimes couple such data with manual observations for validation and comparison, but this approach is costly, only allowing for collection at rare intervals. Where available, CS725 passive gamma radiation SWE sensors can continuously monitor the total water content of the snowpack (Smith et al., 2016). A need remains for detailed depth profiles of storm SWE and snow density as currently, this information can only be determined using primitive snow-pit evaluation tests, often performed long after the avalanche danger has presented itself as an immediate public threat.

To address these challenges, snow depth and SWE data can be ingested into snow-cover models such as SNOWPACK (Bartelt and Lehning, 2002) or CROCUS (Vionnet et al., 2012) that have hazard modules to predict snowpack instabilities. Adoption of these models has been slow due to a combination of mistrust and a significant learning curve (Morin et al., 2020). Moreover, model development has been directed primarily at prediction of persistent weak layers in old-snow.

One model that addresses storm-snow avalanches is the mechanical SNOw Snow Slope (SNOSS) model. The model is based on a stabilityindex first developed by Roch (1966) and Fohn (1966) with later refinements by Jamieson (1995) and Jamieson and Johnston (1998) and evaluation by Conway and Wilbour (1999); Hayes et al. (2004) and Havens et al. (2012). The SNOSS model calculates the ratio of strength to overburden. The shear strength of the storm snow is calculated with a power-law relationship based on snow density, where the storm-snow density is coupled with a densification model for calculating the increase in storm-snow density with time due to metamorphic and overburden stresses. The relationship between the strength of the layer is compared to the overburden weight or the SWE of the overlying snow to determine a "time to failure" (Conway and Wilbour, 1999). Despite the need for real-time forecasting of storm-snow avalanches the model has not been used in operational settings. This is due to a lack of availability of real-time high resolution storm-snow density data, which is the key variable driving the model.

A critical need exists for real-time, observationally-based tools, both hardware and software, that can measure and account for the spatial and temporal variability in atmospheric and storm-snow-related variables found in mountainous terrain, and that can be easily adopted by avalanche forecasters and technicians.

Here we discuss how a new instrument, the Differential Emissivity Imaging Disdrometer (DEID) can be used to help guide snow-cover models. The DEID was developed to capture real-time measurements of snow density, SWE, and precipitation intensity (PI) on a particle-byparticle basis at high temporal resolution (Singh et al., 2021; Rees et al., 2021). Snowflake shape is characterized with a shape density index or SDI and Complexity. In an operational mode, we show how these two variables can be used with the SNOSS model to forecast stormsnow instabilities. Observations collected in Utah's Wasatch mountains during the winter of 2020-2021, and results from the storm-snow instability model, are evaluated and validated against snowpack measurements routinely obtained, such as the Utah Department of Transportation's (UDOT's) Intermountain Labs and Snowbound Technologies Infrasound Detection Systems (Vyas, 2009; Mayer et al., 2020), a highdensity network of standard meteorological stations, and physical observations from snow professionals and recreationalists managed by the Utah Avalanche Center (UAC). The goal is to evaluate the potential contribution to avalanche prediction of real-time measurements of snow density, SWE, and snowflake characteristics. Three main approaches are pursued: (i) investigating the relationships of DEID measurements to stability indices and avalanches, (ii) assessing storm-storm instability with the DEID data and systematic tilt-board tests, and (iii) evaluating a snowpack stability index derived solely from DEID data.

2. Methods

2.1. DEID methodology

A complete description of the DEID is presented in Singh et al. (2021) with additional details given in Rees et al. (2021). Here, we present a concise summary with an update to the physical approach for computing the mass and density of a hydrometeor. The DEID consists of an infrared camera pointed at a hotplate that has low emissivity. To quantify a hydrometeor's size/area on the hotplate, the DEID makes use of the fact that the thermal emissivity of water ($\varepsilon > 0.95$) is very different from that of aluminum ($\varepsilon < 0.1$), such that objects with the same thermodynamic temperature have different radiative temperatures seen by a thermal camera (see Fig. 3). The plate thermodynamic temperature is measured with the thermal camera by placing a high-emissivity ($\varepsilon \approx 0.95$) polyimide tape on the hotplate. The camera records at 15 fps with a resolution 531 pixels × 362 pixels for a spatial resolution of about 0.2 mm/ pixel.

Thermal images of the hotplate provide the area of hydrometeors, the temperature difference between a hydrometeor on the plate and the hotplate, and the evaporation time. Individual hydrometeor mass is determined using the DEID by assuming that the heat gained by a hydrometeor is equivalent to the heat lost by the hotplate during evaporation according to,

$$m = \frac{1}{\left(c\Delta T + L_{eqv}\right)} \int_0^{\tau_{evp}} \left(k/d\right)_{\text{eff}} A(t) \left(T_p(t) - T_w(t)\right) dt. \tag{1}$$

Here, m is the mass of the hydrometeor, c is the specific heat capacity of water, $L_{eqv} = L_v$ is applied for liquid hydrometeors and $L_{eqv} = L_v + L_f$ for solid hydrometeors, where L_f is latent heat of fusion for water and L_v is the latent heat of vaporization of water, T_p is the hotplate surface temperature, T_w is the temperature of the water droplet, and ΔT is the temperature difference between the initial and final temperature of a water droplet on the hotplate. In addition, τ_{evp} is the time required to evaporate the water droplet, and $(k/d)_{\rm eff}$ is an empirical coefficient that has been determined to be 7.006×10^3 W m $^{-2}$ K $^{-1}$. For a snowflake, the SWE may be immediately calculated as, SWE = $(c_1 \Delta m)(A_{hp}\rho_{H_2o})$; c_1 is conversion factor from meters to millimeters (i.e., $c_1 = 10^3$ mm m $^{-1}$), Δm (kg) is the total hydrometeor mass that falls on the hotplate in a given time, A_{hp} (m 2) is a rectangular sampling area on the hotplate and SWE is given in mm of water.

The SWE accumulation rate (R_{SWE}) can be estimated from the total mass of water deposited onto the hotplate in each frame as,

$$R_{\text{SWE}} = c_2 \frac{\Delta m \cdot \text{fps}}{\rho_w A_{hp}},\tag{2}$$

where c_2 is a conversion factor from m s $^{-1}$ to mm hr $^{-1}$ (3.6 × 10 6 mm/h m $^{-1}$ s), fps is the image sampling rate in frames per second, Δm (kg) is the total hydrometeor mass that falls on the hotplate in each recorded frame that is estimated using Eq. 1, ρ_w (kg m $^{-3}$) is the bulk density of water and A_{hp} (m 2) is a rectangular sampling area on the hotplate that captures all hydrometeors. $R_{\rm SWE}$ can also be estimated using a particle-by-particle method whereby Δm in Eq. 2 is the total hydrometeor mass that falls on the hotplate over a given time interval Δt , summed over all individual evaporated hydrometeors.

Snowflake density given by $\rho_s = m/V$, where m (kg) and V (m⁻³) are the mass and volume of an individual snowflake, respectively. Hydrometeor volume V can be estimated by assuming a spherical particle of equivalent circular diameter $D_{\rm eff}$ such that $V = (\pi/6)D_{\rm eff}^3$ (Rees et al., 2021). However, since snow particles are typically aspherical, a methodology for estimating density based on the heat flux to a hydrometeor (that is independent of shape) was developed (Singh et al., 2023). The heat flux from the hotplate into a single snowflake is,

$$E = \frac{H}{A_e \tau_{evp}},\tag{3}$$

where A_e is the maximum observed area of the snowflake on the hotplate before it evaporates. $H=mL_{eqv}$ is the total energy required to melt and evaporate the snowflake from the hotplate. From observations, we find that for a given area and evaporation time, multiple values of E can be obtained for a given value of snowflake mass due to varying amounts of liquid water, suggesting a correlation between snowflake density and the heat flux. Thus, we hypothesize that the heat-flux method can be used to compute the density of different types of snowflakes through comparison to a reference as follows,

$$\rho_s = \rho_0 \frac{E}{E_0}. (4)$$

Values for ρ_0 and E_0 were determined from field measurements and validated in laboratory experiments. The average density $(\overline{\rho}_s)$ prior to settling over a given period can be calculated from DEID data using the ratio of the total mass to total volume in a given time interval, namely,

$$\overline{\rho}_s = \frac{\sum_{i=1}^N m_i}{\sum_{i=1}^N m_i / \rho_{s,i}},\tag{5}$$

where m_i (kg) is the mass of the i^{th} snowflake, $\rho_{s,i}$ (kg m $^{-3}$) is the density of the i^{th} snowflake and N is the total number of snowflakes on the plate measured during the given period. From the average density of the snowflakes in each frame, the snow precipitation rate or precipitation intensity (in mm h $^{-1}$) is,

$$PI_{snow} = c_2 \frac{\Delta m \cdot \text{fps}}{\overline{\rho}_+ A_{hp}}.$$
 (6)

Note that the difference between the calculation of PI_{snow} and R_{SWE} is the average density of the phase of the evaporating hydrometeor in the denominator in Eq. 2 and Eq. 6, namely ρ_w for R_{SWE} and $\overline{\rho}_s$ for PI_{snow} . Total snow accumulation, HST (mm), is then computed by multiplying the precipitation rate by the time interval between samples (1/fps), then summed over the period of interest such as for a storm or every hour.

2.2. Instability model

The evolution of fresh snowpack instability can be determined using DEID measurements in combination with a simple physics-based model, such as the SNOw Slope Stability model (SNOSS) (Hayes et al., 2004). A

stability index can be defined as the ratio of the strength of a buried layer to the shear stress imposed by the overburden stress from the snowpack above, such that the snowpack becomes unstable when the stability index value approaches and falls below unity (Conway and Wilbour, 1999; Hayes et al., 2004; Havens et al., 2012). Fig. 1 is a schematic of storm snow over old snow and the corresponding coordinate system used herein. In order to evaluate the stability index, the following parameters are required: the shear strength of the buried layers, which depend on grain shape, type, and density of the grain, and the imposed shear stress from the weight of the overburden, adjusted for slope angle for the terrain of interest. Following Jamieson and Johnston (2001), the shear strength (in kPa) of a buried layer ($\alpha(z,t)$) at a depth z and at time t after the snow begins to accumulate is expressed as,

$$\alpha(z,t) = \lambda \left(\frac{\rho_s}{\rho_s}\right)^{\beta},\tag{7}$$

where $\rho_s(z,t)$ is the density of a given snowpack layer, ρ_i is density of ice ($\rho_i = 917 \text{ kg m}^{-3}$) and λ and β are empirical constants that depend on the ice-grain form. This formulation is related to the Young's modulus of ice, which provides a power-law behavior that is supported through manual observations (Perla et al., 1982; Jamieson, 1995). Traditionally, λ and β are determined by fitting experimental measurements of the shear strength of precipitation particles performed using a strain gauge. In the present work, we use two sets of precipitation-particle values. The first are values recommended by Jamieson and Johnston (2001): $\lambda = 5.32 \text{ kPa}$ and $\beta = 1.35$, and the second are DEID-derived values that are explained in Sec. 2.5. Results from both methods are computed (a) assuming a constant density in time and (b) using a densification model, using four different shear-strength models. The four models, shown in in Table 1, suggest a possible range for forecasted stabilities that may help increase predictive accuracy through ensemble averaging.

Over the course of a storm, each layer of buried storm snow increases in density through metamorphic stresses in addition to stresses from the gravitational component of the overburden weight $(\sigma_{zz}(t) = g \int R_{SWE-\cos^2\theta} dt)$. For simplicity, the metamorphic stress $(\sigma_m(t))$ is assumed to be a constant (75 Pa) and is added to the overburden stress (Conway and Wilbour, 1999). This value assumes that the near-surface (5–10 cm) densification of the storm snow is dominated by metamorphic stress, but is driven by the gravitational component for layers that are deeper than 5 to 10 cm from the surface. By assuming a viscous densification law for dry storm snow, the density of the snow $(\rho_z(t))$ can be expressed at each layer and point in time by the following ordinary differential equation:

$$\frac{1}{\rho_z(t)}\frac{d\rho_z}{dt} = \frac{1}{\eta_{zz}} \left[\sigma_m(t) + \sigma_{zz}(t)\right]. \tag{8}$$

Here, $\eta_{zz}(t)$ represents the compactive viscosity for dry snow, which was experimentally determined by Kojima (1967) and modified with an Arrhenius-type temperature term by Conway and Wilbour (1999),

$$\eta_{zz}(t) = B_1 e^{B_2 \left(\frac{\rho_z(t)}{\rho_i}\right)} e^{E/RT_z}.$$
(9)

The following constants, $B_1=6.5\times 10^{-7}$ Pa s, $B_2=19.3$, the activation energy $E=67.3~{\rm kJ^{-1}}~{\rm mol^{-1}}$, the universal-gas constant $R=0.008314~{\rm kJ^{-1}}~{\rm mol^{-1}}~{\rm K^{-1}}$, and the layer temperature $T_z=273~{\rm K}$ were utilized in the calculation of η_{zz} . Eqs. 8 and 9 can be discretized and solved with a simple Euler's method for an initial density profile provided by the DEID. Thus, with a coupled model and DEID data, a high-resolution map of snow-layer density can be obtained that is a function of time. It should be noted that the compactive viscosity (η_{zz}) and the metamorphic stresses (σ_m) were derived for dry storm snow and may need to be altered for wet or mixed precipitation particles.

The overburden stress (W), or the average static shear stress on terrain with a slope angle (θ), is expressed as,

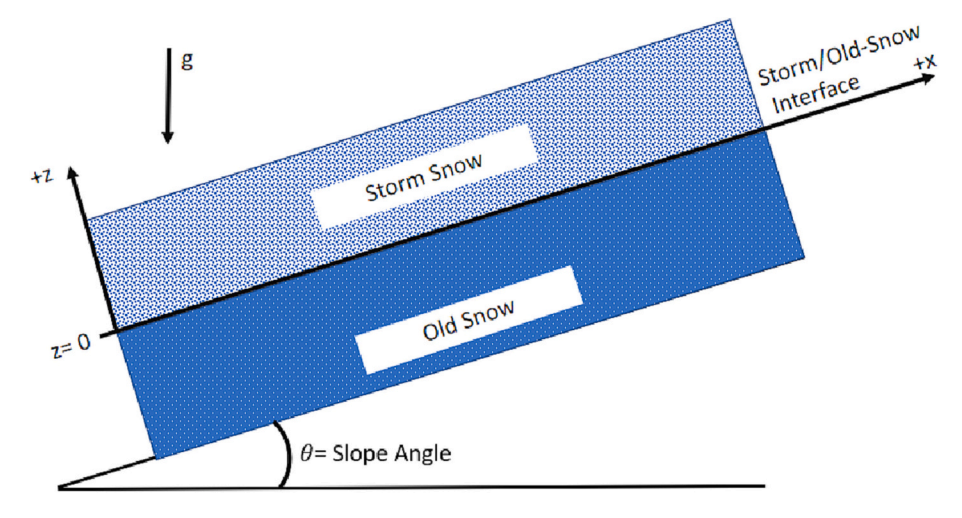


Fig. 1. Coordinate convention reference for a storm-snow avalanche on a slope with an inclination angle θ .

Table 1A summary of the four model variations evaluated during the study as well as the ensemble of the models.

Model	λ (kPa)	β	Description
Jamieson 2001, no densification	5.32	1.35	Constant coefficients of strength
Jamieson 2001, with densification	5.32	1.35	Constant coefficients of strength
SDI & Complexity, no densification	SDI	Complexity	Coefficients are a function of snowflake structure
SDI & Complexity, with densification	SDI	Complexity	Coefficients are a function of snowflake structure
Ensemble	-	-	Average of all model outputs

$$W(z,t) = g \int_0^t R_{\text{SWE}}(t) \sin(\theta) \cos(\theta) dt, \tag{10}$$

where $R_{SWE}(t)$ is SWE rate at time t. Hence, the stability index (SI) is the ratio of the shear strength (Eq. 7) to the overburden stress of the overlaying snow (Eq. 10),

$$SI(z,t) = \frac{\alpha(z,t)}{W(z,t)}.$$
(11)

For values of SI \gg 1, the snowpack is expected to be stable, and for SI \leq 1, instability is anticipated. The DEID provides real-time values of $\rho_{\rm S}$ and $R_{\rm SWE}(t)$ so that the stability index can, for the first time, be calculated in real-time during a storm to forecast time to failure within stormsnow layers.

$2.3. \ \ New\ microphysical\ parameters:\ SDI\ and\ complexity$

We now introduce two new parameters, the hydrometeor shape density index (SDI) and the Complexity, that can be easily measured with the DEID for classification of precipitation particle type. SDI is defined as the ratio of the cross-sectional snowflake area A_e on the hotplate to the melted area of a spherical water droplet A_{H_20} that has the same mass (Eq. 12),

$$SDI = \frac{A_e}{A_{H-O}}.$$
 (12)

The melted area of a spherical droplet of the same mass can be expressed (after some algebra) as,

$$A_{H_20} = C_{\text{SDI}} \left(\frac{m}{\rho_{H_20}} \right)^{2/3}. \tag{13}$$

Here, $C_{\rm SDI}=1.21$ is a geometric constant, m is the mass of the snowflake, and ρ_{H_20} the density of liquid water, which is taken to be 1000 kg m⁻³. A schematic showing the method of SDI calculation is supplied in Fig. 2. The minimum value of SDI is near unity for spherical snow particles that have a density close to water.

Particle Complexity is defined as the ratio of the area of the smallest ellipse containing a particle cross-section to A_e of the hydrometeor measured on the hotplate as illustrated in Fig. 3. The areas used to calculate each individual particle's Complexity and SDI are determined here using Matlab's image processing toolbox, Regionprops (MajorAxisLength and MinorAxisLength),

$$Complexity = \frac{\pi ab}{A_e},\tag{14}$$

where a and b are the major and minor axis length of ellipse that fit over the snowflake. The minimum value of Complexity is unity for a circular snow particle. Differences between definitions for derived region properties inside language-dependent image-processing tool boxes may lead to slight differences in the derived ellipses of the particles.

2.4. Identification of snowflake habit using SDI and complexity

A laser-SLR camera system, which provides images of falling snow-flakes is used to correlate DEID measured variables to snow-crystal type. A 7-cm thick laser sheet for illuminating snowflakes was generated by merging three green 10-W lasers (520 nm wavelength) and then focusing the laser into a plane with spherical lenses. High-resolution images of snowflakes were acquired using a Nikon D850 SLR camera with a Nikon AF-S VR Micro–Nikkor 105 mm f/2.8 G IF-ED lens. The

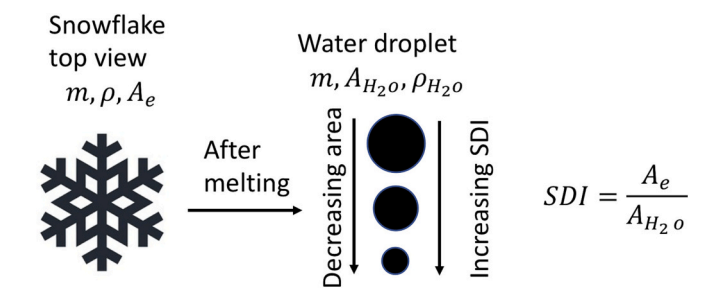


Fig. 2. Physical and mathematical interpretation of snowflake SDI. A_e is the cross sectional area of snowflake, A_{H_20} is the area of spherical water droplet after melting. The down arrow indicates decreasing water droplet area after melting (a smaller area for less dense snowflakes). Less dense snowflakes have a higher SDI.

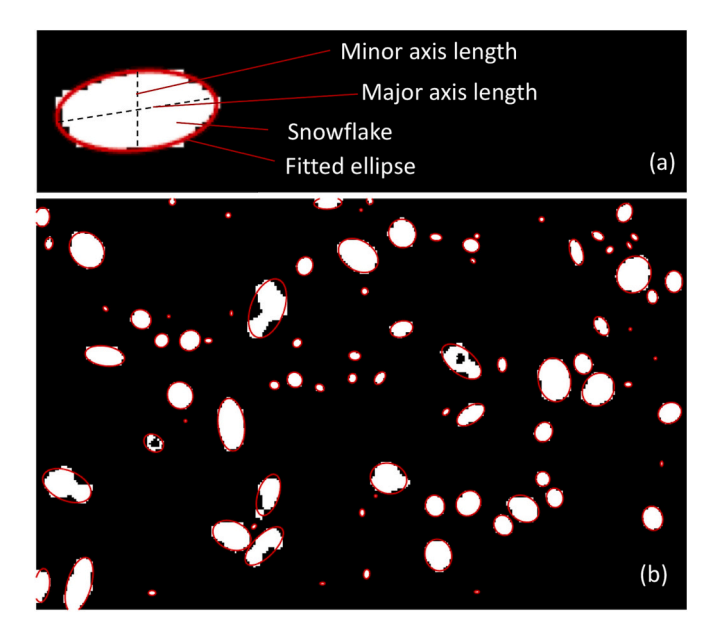


Fig. 3. (a) Illustration of the major-axis length and minor-axis length of the ellipse fit over a snowflake; (b) a black and white image showing melting snowflakes on the hotplate of the DEID as seen by the thermal camera during a snow event. Using Matlab's image-processing toolbox, the DEID tracks individual hydrometeors as they impact the hotplate, melt, and evaporate. Through tracking this process and measuring the snowflake area, as well as the area of the ellipsoid containing the snowflake, the SDI and Complexity are derived. Note that potential differences between language-dependent image-processing tool boxes may lead to slight differences in the derived ellipses of the particles.

laser sheet is oriented such that falling snowflakes are imaged as they enter the light-sheet plane. The bottom of the laser sheet was situated about 2 cm above the hotplate of the DEID so that 2-D images of falling snowflakes obtained by the SLR camera could be directly correlated with DEID measurements. The type of snowflake crystal was categorized based on the international classification for seasonal snow on the ground (Fierz et al., 2009). We categorized six habits of the snowflake (Praz et al., 2017), planar crystal (combining stellars and plates), graupel (combining hail and graupel), columnar crystal, irregular crystal, aggregate and small particles. Irregular crystals and aggregates were separated by their aspect ratio due to their anticipated structural differences, with columns aggregating more spherically and plates more elongated (Dunnavan et al., 2019).

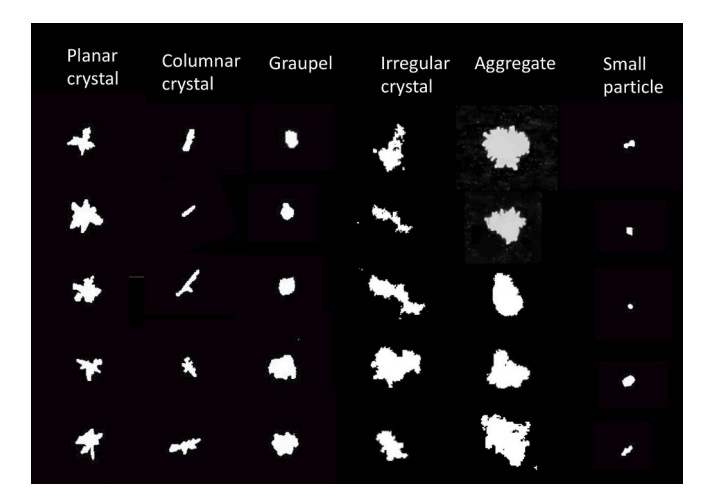


Fig. 4. Various snowflake images obtained from the SLR camera taken at the Alta-Collins snow-study plot. Black and white images of six types of snowflakes are illustrated. Each type consists of five samples.

Fig. 4 shows example images of the six different hydrometeor types. As snowflakes rotate as they fall in the laser plane, an advantage of the classification technique is that snapshots are obtained from multiple angles of each hydrometeor without necessitating use of multiple cameras, as is the case for devices such as the Multi-Angle Snowflake Camera (Garrett et al., 2012). Identification of crystal type was based on all images of individual snowflakes captured by the SLR to represent one type of crystal. After landing, the SDI and Complexity of each type of crystal are calculated using the measured mass and area of an individual snowflake from the DEID. For each snowflake habit, 21 samples were taken and correlated with the corresponding SDI and Complexity. This process was done by visually inspecting individual snowflakes (Fig. 4). A summary of snowflake habit as a function of SDI and Complexity is provided in Table 2. Due to the limited number of samples, some overlap between classifications exist. Further studies are underway to refine the classification technique.

2.5. Relating SDI and Complexity to shear strength

Extensive past research has examined the shear strength of buried old-snow-layer crystal structure as a function of density and grain type (Schweizer et al., 2006). Casson, Stoelinga and Locatelli (2008) explored the importance of storm-snowflake habit on the shear-strength relationship with data collected from Snoqualmie Pass. Their work revealed that simple shear-strength parameterizations that only consider the density for precipitation particles may oversimplify the intricacies of the strength of each snowflake habit. In other words, different snowflake habits may lead to different bonding or interlocking between snowflakes and therefore affect the overall shear strength. For example, we anticipate that dendrite-dendrite and needle-needle bonding differs and is both a function of density and snowflake habit. Based on our work linking SDI and Complexity to snowflake habit, we hypothesize that the coefficients of strength can be substituted with these variables such that $\lambda = c_3 \text{SDI}$ (with units of kPa through multiplying by conversion factor c_3 = 1 kPa) and β = Complexity (unitless).

To test this hypothesis, we calculate the mean of SDI and Complexity for 5 mm deep freshly-fallen snow layers and calculate the shear strength from Eq. 7. The habit for each 5 mm layer is computed by averaging the Complexity and SDI for each layer and determining the snowflake habit following Table 2. The calculated shear strengths is then compared against the standard fixed-coefficient models from Jamieson and Johnston (2001), Conway and Wilbour (1999), Brun and Rey (1987), and Perla et al. (1982) (Fig. 5). We find fair agreement and behavior (increasing strength with increasing density) between the newly propose SDI and Complexity model and the accepted models; hence, we further explore the utility of SDI and Complexity in the text that follows.

2.6. Experimental site and setup

Data were collected from 2020 October to 2021 May in Upper Little Cottonwood Canyon, Utah, USA at the Alta Ski Area mid-Collins Snow Study Plot (40.5763° N, 111.6383° W, 2920 m above sea level). The mid-Collins Snow Study Plot is $\sim\!24$ m wide from east to west and 45 m from north to south. The plot is roped off and off-limits to resort guests,

Table 2Preliminary estimates of the relationship between SDI, Complexity and snow-flake crystal subclass.

Crystal Subclass	SDI - λ (kPa)	Complexity - β
Planar crystals	6.12–14.89	1.21-1.53
Columnar crystals	13.65-19.89	1.41-1.59
Graupel	3.21-6.53	1.10-1.18
Irregular Crystals	16.23-21.83	1.31-1.49
Aggregates	18.75-28.30	1.18-1.34
Small particles	2.11-8.96	1.00-1.21

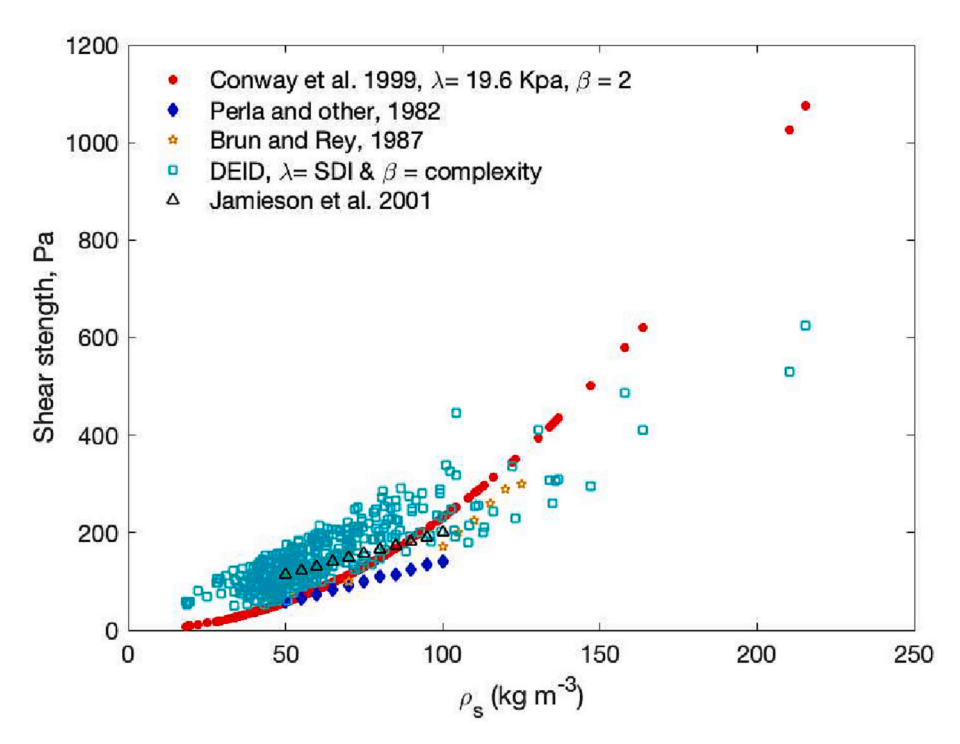


Fig. 5. Shear strength of snow layers (each 5 mm thick) as a function of snow density using Eq. 7, where λ and β are SDI (kPa) and Complexity (unitless), respectively and are compared with previously reported shear strength for weak layers by Conway and Wilbour (1999) – red solid circles, Perla et al. (1982) – blue solid diamonds Brun and Rey (1987) – hollow stars and Jamieson and Johnston (2001) – black hollow triangles. (For interpretation of the references to colour in this figure legend, the reader is referred to the web version of this article.)

so the snow surface remains protected and undisturbed. The study plot is surrounded by trees and open to the sky, providing an ideal setting for measuring snowfall. At a larger scale, the study plot sits in the Collins drainage, surrounded by Mt. Baldy (elevation of 3374 m) to the southwest, with extending ridge lines to the north that decrease in elevation to the highway (Utah SR-210). For further details, see Fig. 6a, which provides a topographic map of the area around the study site (red star).

Fig. 6b shows the DEID and supporting instrumentation. The apparatus was placed on a permanent 6 m tall, $10.16~\rm cm \times 10.16~\rm cm$ square steel box-section tower with two pulleys/winches mounted to a concrete base, which allowed the experimental apparatus to be raised and lowered as snow accumulated throughout the winter. A mounting system constructed from $80/20~\rm T$ -slot aluminum (Columbia City, Indiana, USA)

was fixed to the pulley/winch system on the tower. The DEID was attached to the mounting system, suspended in the air and off the snow surface, allowing for direct snowfall onto the hotplate. The DEID's individual components were all carefully connected to the 80/20 aluminum frame. The DEID consists of a hotplate with a feedback controller and a thermal camera pointing at the hotplate. The hotplate is a Systems and Technology International, Inc. HP-606-P. The custom hotplate has a heated area of 0.1524 m \times 0.1524 m and a thickness of 0.0508 m. Note the thermal camera sampling area of the hotplate is 6.5 cm \times 8.7 cm and is powered by a 120 V, 5 Amp supply with a digital proportional-integral-derivative (PID) feedback control mechanism to control the plate temperature. The top plate surface is composed of a 6061 aluminum alloy with a thermal conductivity, $k=205~{\rm W~m}^{-1}~{\rm K}^{-1}$

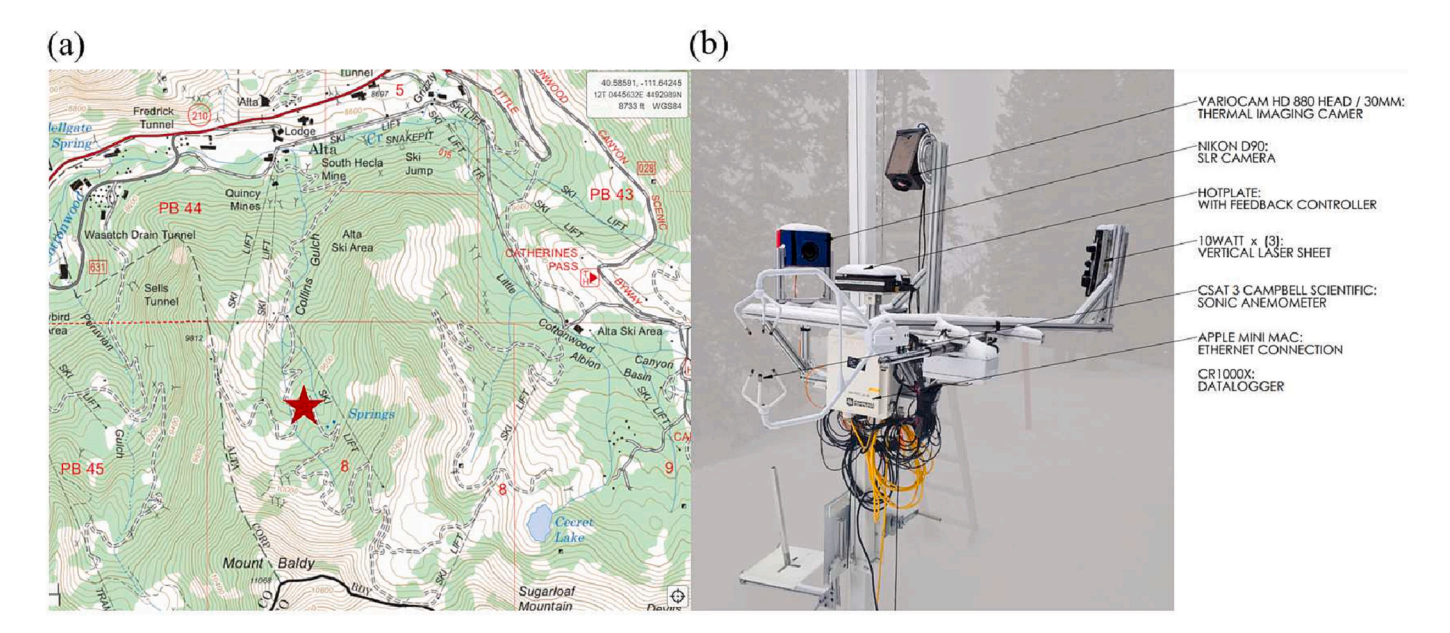


Fig. 6. (a) Topographic map showing the location of the Alta Ski Area mid-Collins Snow Study plot marked with a star and (b) photograph of the DEID experimental setup during Winter 2020–2021.

which was roughened using 2000 grit sandpaper in a linear motion across the plate yielding long straight grooves. To maintain strong thermal contact, the aluminum plate was fixed to the top of the heater with thermal paste. A piece of Kapton® tape with high total hemispherical emissivity (ε =0.95) is affixed to the top of the aluminum plate to measure the actual surface temperature using the thermal camera. The maximum operating temperature of the hotplate for Alta field experiments was 106 °C. The thermal camera used for all experiments is an uncooled microbolometer Infratec Vario HD 700 thermal camera with 432 \times 288-pixel resolution, sampling at a rate of 15 Hz. Note that the thermal camera only measures the correct temperature of the surface when the emissivity of the plate surface is high (i.e, when a hydrometeor lands on the surface). Otherwise, the low emissivity of the plate surface renders the background brightness temperature small.

In addition to the system's main components, Alta Ski Area provided a wired ethernet connection that enables rapid transfer of images from the computer located at the study plot to a workstation at the University of Utah where post processing of the images occurred. Storms were delineated by continual monitoring of the National Weather Service and University of Utah forecasting products (https://weather.utah.edu/). Prior to the onset of snowfall the DEID was turned on and would collect data until precipitation stopped. During these events data transfer was performed every 1 h, corresponded to approximately 1.2 GB of data. During winter 2020–2021, images were downloaded in batches during or after the storm and processed with a Matlab script described in Singh et al. (2021).

To compliment this deployment, we made use a wide variety of snow-measuring instruments and manual-observation boards that are routinely deployed and maintained by the Alta Avalanche Office at the mid-Collins study plot. The observation boards used included three main manual snow measuring boards that are used for measuring the amount of snowfall at different time intervals during a storm, specifically at 12 h, 24 h, and at the end of the storm duration. These snow boards are 30 cm \times 30 cm with a 60 cm long measuring stick projecting from the center of the board. The Alta Avalanche Office visits the site at each time interval and records the height of snow measurements and uses a Snowmetrics snow density kit containing a spring scale, tube, and scraper to measure the density and weight of the storm snow. The weight and density measurements acquired from these boards were used to validate those same measurements from the DEID. The site also has four automated snow measuring devices, including a NOAH II all-weather precipitation gauge from ETI instruments and a Novalynx rain gauge. This instrument collects and records the weight of the storm snow and generates automated hourly SWE data that are transferred to Mesowest (thttps: //mesowest.utah.edu), making the data easily accessible. Additionally, the site has three Campbell Sci. Inc. SR50 ultrasonic snow-depth sensors that record the height of snow and automatically upload the data to Mesowest every hour. These SR50 sensors also measure running totals on a 12 h, total depth, and a storm frequency. Lastly, the site also has a live camera pointed at another 12 h snowboard that is illuminated with lights for 24 h recording.

2.7. Snowboard tilt tests

To better understand the relationship between the DEID's density profiles and storm-snow instability, we designed a repeatable shear-stability test based on standard tilt-board and shovel-tilt tests. A tilt-board stability test is an easy method to quickly identify unstable layers in storm snow (Schweizer et al., 1998). The basic method was first developed over fifty years ago by Schleiss and Schleiss (1970) to investigate shear instabilities in storm snow. As described by McClung and Schaerer (2006), a tilt-board test makes use of an isolated 30 cm \times 30 cm block of snow, no >40-cm deep that is placed on a metal plate. The plate is transferred to a horizontal board that pivots to 15° . The plate is tapped when at 15° until failure and the location of the failure plane is measured. The standard field variant of the method, the *shovel tilt test*,

isolates an approximately $30 \text{ cm} \times 30 \text{ cm}$ column (again, no thicker than 40 cm) on a shovel which is tilted at 15° and then tapped until shear occurs; tests are rated as Easy, Moderate, or Hard (Greene et al., 2004).

The tilt board used in our study, shown in Fig. 7, is a modified version of the standard method described above. We used a Snowmetrics snow board which is made of plastic and is 41 cm \times 41 cm \times 1.25 cm. We placed the snow board on an 80/20 T-slot aluminum frame that affixed to the same crank-up mast as the DEID. Alta Ski Patrol used this modified tilt board test every 12 h during their morning and afternoon observations at the mid-Collins Study Plot.

Alta Ski Patrol kept the snow board as close to the ground as possible to avoid wind and other factors altering the natural snowfall. They used the following methodology: 1) Using a snow-saw, an initial cut was made around the storm snow, taking care not to disturb the test sample. Once complete, the remaining test slab had the same dimensions as the snow board. 2) Using the hand crank on the tower, the snow board was then raised off the ground to a height where the tilt of the board could be positioned to 30° . 3) The test would then begin with taps from the wrist and continue until there was a shear failure within the storm snow; 'no failure' was recorded if there was no failure reported after 30 taps. 4) A detailed record of the test was saved and if possible the grain type in the the failure plane was recorded. This sequence would repeat every 12 h with storm snow at approximately 04:00 and 16:00 LT.

2.8. Infrasound and Utah Avalanche Center observations

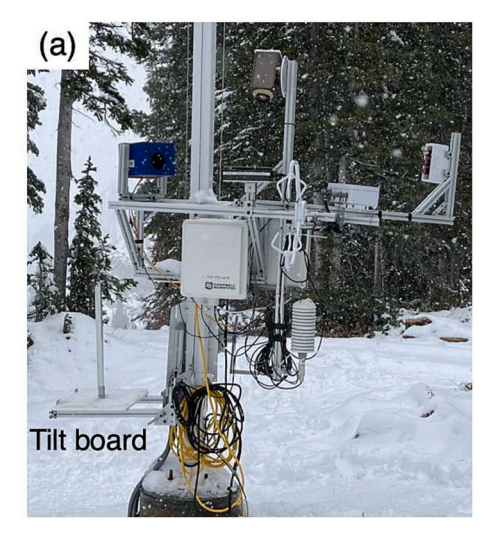
To aid in the validation of the storm-snow instability model, we used data collected from UDOT's infrasound detection systems (Vyas, 2009; Mayer et al., 2020). The infrasound systems in LCC are produced by Intermountain Labs and Snowbound Technologies and are deployed in all prominent slide paths within LCC. The systems detect the precise timing and location of avalanches by listening for the low frequencies generated by avalanches in motion. Once an avalanche is in motion, the infrasound systems detects the frequency and gives specific details about the avalanche, time in motion, power, and where it started and ended. To provide a larger picture of the avalanche activity in LCC and the surrounding region, the storm-snow instability model was assessed using observational data collected by the UAC through a web portal submitted by recreationalists and snow professionals. Data for this study can be found through their online archives (https://utahavalanchecenter.org/avalanches).

3. Results

3.1. Stability results

Over the course of the winter, the DEID captured data from numerous storms. For this report, data from fourteen storms occurring between 12 December 2020 and 26 April 2021 are presented. To understand the conditions and avalanche hazards after each storm, data collected from the DEID, the infrasound detection system, and visual observations from the UAC were combined. A summary of these results can be found in Table 3. Table 3 provides details on the storm start time, end time, total snow accumulation, total SWE, max SWE rate, mean and range of storm-snow density, maximum density gradient in the storm snow, and the ensemble averaged stability index from the four members of the model. It should be noted that all of these variables are measured directly or derived solely from DEID observations. The columns that follow the DEID-derived data provide insight into the avalanche conditions in the Central Wasatch Mountains from tilt-board test results at the mid-Collins site, time of first infrasound avalanche detected in LCC, and post-storm 3-day total number of avalanches in the Central Wasatch.

Of the fourteen storms observed and reported in Table 3, three storms from the 2020–2021 season were identified for density profiles and forecasted storm-snow avalanche problem as noted by the UAC and post-storm activity. Data collected by the UAC can be found in their



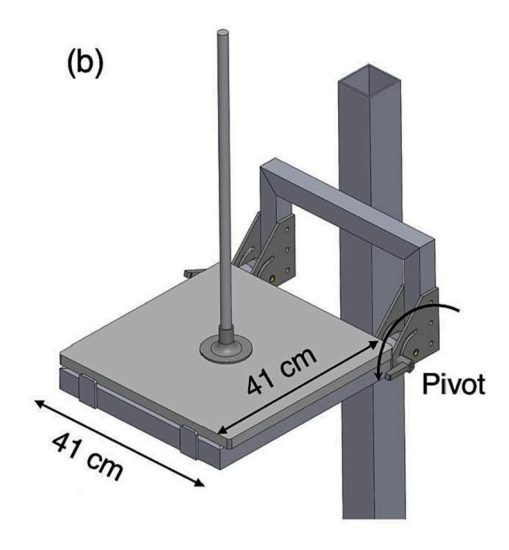


Fig. 7. (a) Tilt board deployed in the field with the DEID (b) SOLIDWORKS rendering of the tilt board.

Table 3
Table of DEID measured parameters and snow stability metrics during winter 2020–2021 for ten different snow events observed in Little Cottonwood Canyon. Tilt board test are "POS" or "NEG" for positive or negative results, and if a positive result occurs, the number of taps are shown. Infrasound - indicates if infrasound results were positive and when. UAC observations indicate the total number of avalanches reported during that period and the number of trigger types in the format unknown/user/natural/explosive. Natural avalanches are in boldface type. NA indicates data "not available".

Storm-Snow Stability Metrics										
Storm Start Time/Day (MST)	Storm End Time/Day (MST)	Total Snow (mm)	Total SWE (mm)	Max SWE Rate (mm/h)	$\overline{\rho}$ (kg/m ³ , range)	$\frac{\delta \rho}{\delta z}\Big _{max}$ (kg/m ⁴)	SI_{min}	Tilt Board Test	Infrasound	UAC Observed Avalanches
0100 12/12	2000 12/12	292	10.66	5.16	34 [12,190]	17	1.30	NA	NEG	5 (1/3/1/0)
1917 12/13	0830 12/15	147	10.34	2.57	72 [11,238]	- 130	6.55	NA	NEG	8 (0/8/ 0 /0)
0600 12/17	0700 12/18	413	27	11.24	63 [13,266]	200	1.22	NA	POS: 0025 12/18	41 (7/16/18/0)
0900 12/22	0900 12/23	314	15.38	31	54 [19,214]	12	1.14	NA	NEG	11 (5/4/2/0)
0845 01/22	0600 01/24	457	34.37	50	71 [21,420]	- 29	0.96	NA	NEG	27 (5/12/10/0)
0600 02/03	2000 02/05	488	31.75	28.93	70 [11,275]	200	1.29	POS	POS: 1515 02/05	34 (4/6/ 24 /0)
2125 02/11	1600 02/14	862	51.81	8.91	57 [16,266]	56	0.91	POS	POS: 0244 02/12	155 (10/5/ 72 /69)
0000 02/15	2000 02/17	1078	65.15	29	57 [12,309]	178	0.47	NA	POS: 0058 02/16	114 (4/1/ 55 /54)
1611 02/26	1600 02/27	402	24.13	13.01	59 [13,187]	76	1.50	NA	POS: 0730 02/27	12 (2/5/5/0)
0743 03/20	2000 03/22	598	33.35	9.11	50 [14,495]	22	1.39	POS	POS: 0735 03/21	8 (2/4/2/0)
0715 03/25	0600 03/26	323	16.79	24.02	54 [15,432]	53	3.79	NA	NEG	10 (1/4/5/0)
1727 04/13	2052 04/14	628	40.49	43.99	66 [18,342]	55	0.83	NA	NEG	13 (3/7/3/0)
0222 04/15	2310 04/15	352	20.84	11.95	42 [12,187]	230	1.57	NA	NEG	17 (3/11/ 3 /0)
0433 04/26	1300 04/26	272	35	11.4	83 [23,488]	- 180	1.43	NA	NEG	7 (2/4/1/0)

digital archives at utahavalanchecenter.org. These storms can be summarized as follows:

- 1. 12 December 2020: Avalanche observations indicated that one natural avalanche occurred in the storm snow and three user-triggered avalanches occurred; the forecast demonstrated that the storm snow was sensitive to skier-triggering following the storm through photos and videos. Report details can be found at https://ut ahavalanchecenter.org/forecast/salt-lake/12/13/2020.
- 2. **27 February 2021:** Avalanche forecasts for the region were for storm and wind-transported snow at mid to upper elevations. One notable skier-triggered avalanche was on steep southeast-facing terrain, which broke 300–450 mm from the snow surface. Report details can be found at https://utahavalanchecenter.org/forecast/salt-lake/2/28/2021.
- 3. **20 March 2021**: For this case, two natural avalanches and four skiertriggered avalanches that were 300–450 mm deep and that failed in the storm snow were reported. Report details can be found at https://utahavalanchecenter.org/forecast/salt-lake/3/22/2021.

To better understand the DEID-based instability model presented in Section 2.2, detailed results from the stability model are supplied in Figs. 8 through 13. These results are solely produced by the DEID and highlight the input, derived, and final variables (outputs) for each of our three case studies described above. The results and figures serve as potential tools that could be used to produce real-time forecasting scenarios. Figs. 8, 10, and 12 show results for the model run with coefficients derived from Jamieson and Johnston (2001) coupled with the Conway and Wilbour (1999) densification model. Other modelmember results are not shown since they show similar trends for each case. For each case, subplot (a) shows a density profile of the snowfall

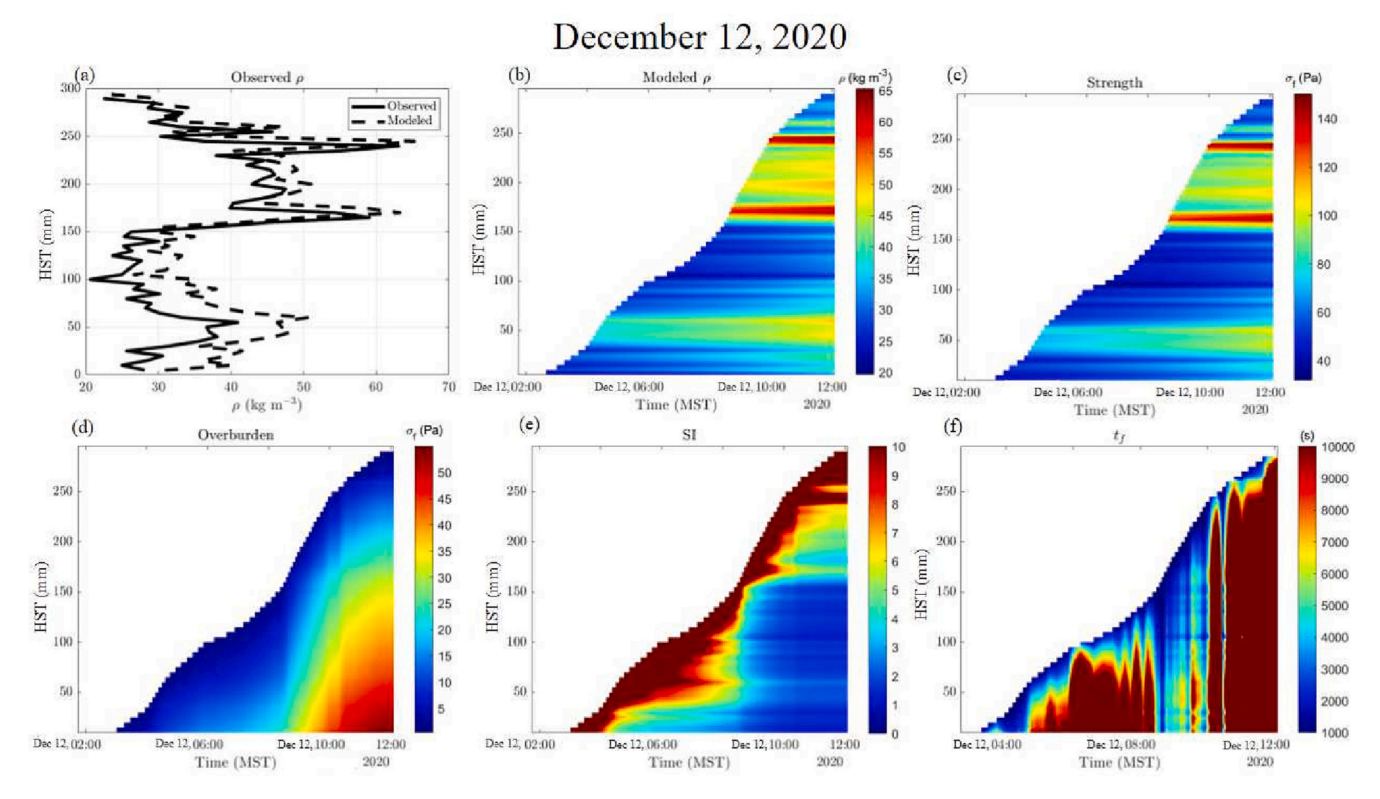


Fig. 8. Avalanche forecasting plots produced with data from the DEID for storm beginning on 12 December 2020. (a) The measured and modeled density profile of the storm snow, (b) The modeled storm-snow density over the course of the storm, (c) the modeled shear strength of the storm snow, (d) the measured overburden force of the storm snow, (e) the stability index (ratio of subplot c to subplot d), and (f) the predicted time to failure in seconds of the storm snow.

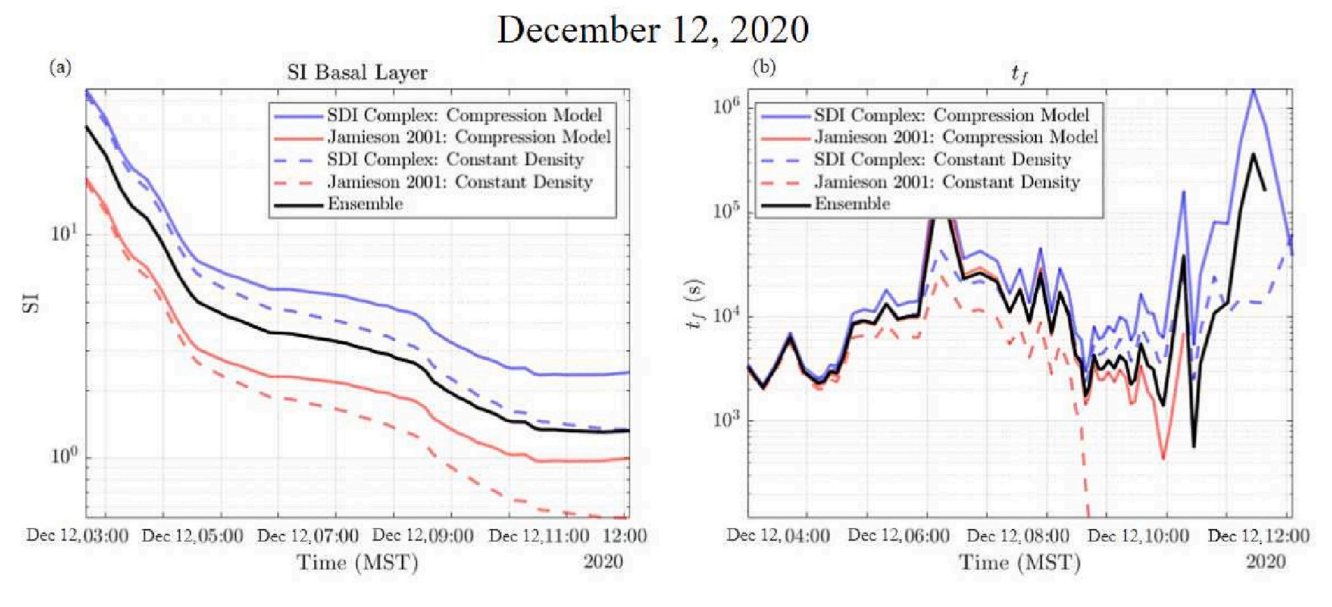


Fig. 9. Storm-snow/old-snow interface plots of (a) stability index (SI) and (b) the time to failure (t_f) for storm snow data beginning on 12 December 2020.

during the storm (solid line) and a density profile of the storm snow at the end of storm computed with the densification model. Subplot (b) is the storm-snow density showing its evolution/densification over the time of the storm, which is used to compute the storm-snow strength over time (c) and overburden (d). Lastly, subplots (e) and (f) present the stability index (SI), which is the ratio of subplot (d) to (c), and the time to failure, computed following the method of Conway and Wilbour (1999).

Figs. 9, 11, and 13 provide the stability index and time to failure at

the interface between the old snow and storm snow using the four variations of the stability model presented in Table 1 and an ensemble of all model's outputs. The approach of presenting an ensemble of models is akin to the weather forecasting approach where multiple models with a variety of initial conditions are supplied to statistically understand the agreement of multiple models. It should also be noted that this figure can be produced for any storm layer of interest, but the interface between the old snow and storm snow is discussed here for simple interpretation of the results.

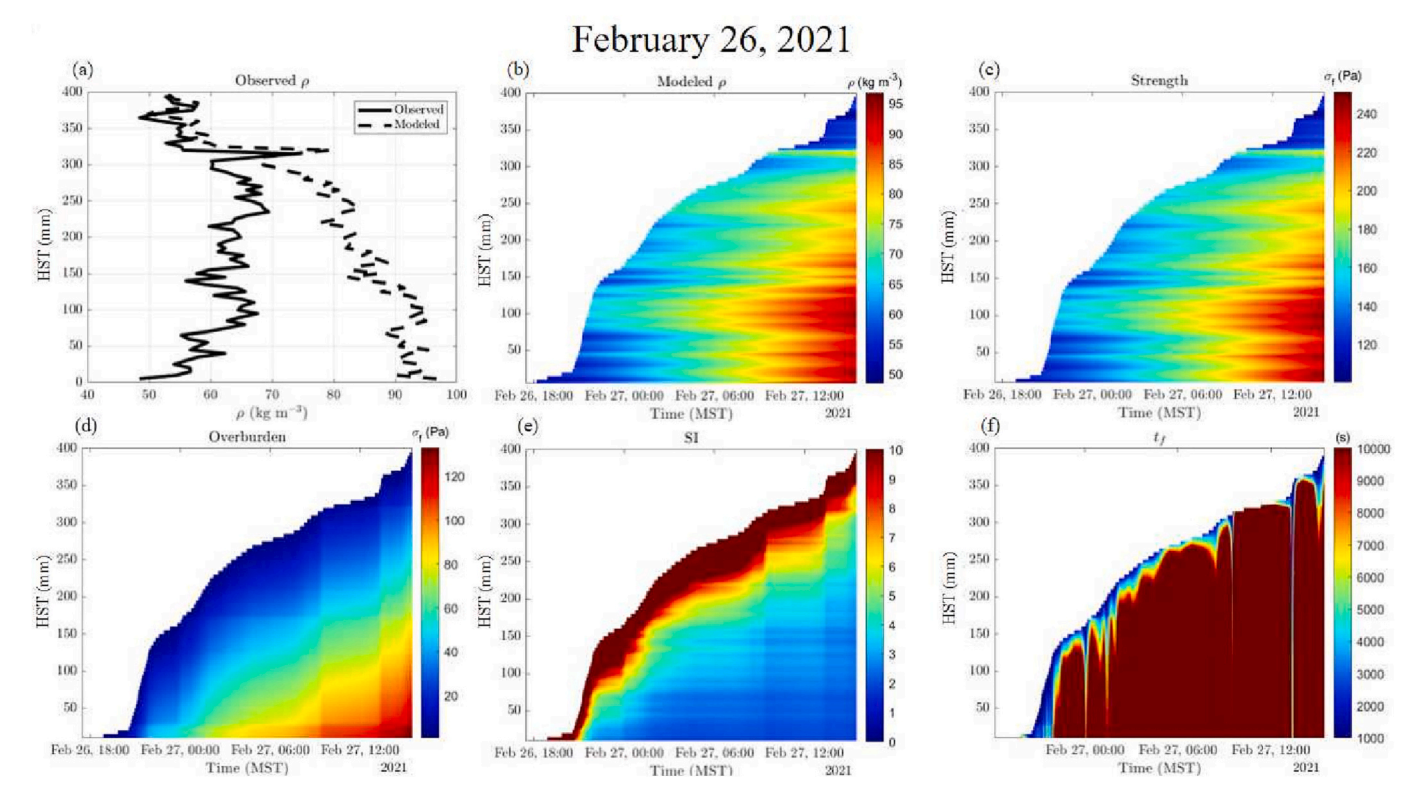


Fig. 10. Avalanche nowcasting plots produced with data from the DEID for a storm beginning on 26 February 2021. (a) The measured and modeled density profile of the storm snow, (b) Modeled storm-snow density over the course of the storm, (c) the modeled shear strength of the storm snow, (d) the measured overburden force of the storm snow, (e) the stability index (ratio of subplot c to subplot d), and (f) the predicted time to failure in seconds of the storm snow.

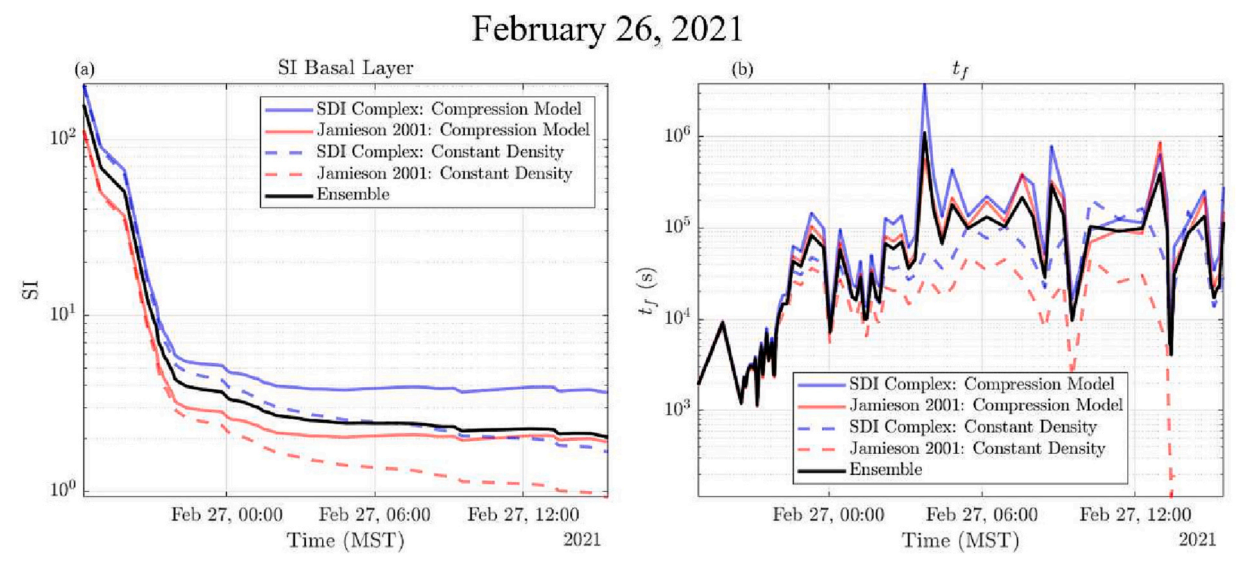


Fig. 11. Storm-snow/old-snow interface plots of (a) stability index (SI) and (b) the time to failure (tf) for storm snow data beginning on 26 February 2021.

Details from the storm on 12 December are shown in Figs. 8 and 9. This storm produced 292 mm of snow and 10.7 mm of SWE (Table 3). Initial density profiles from the storm snow (Fig. 8a and b) show low-density (20–30 kg m³) snow in the lowest 150 mm with higher-density snow (60 kg m³) above these layers at 50 mm and from 150 mm to 200 mm. This high level of detail in the storm-snow density in-dicates the existence of slight density inversions, which are also present in the strength profile (Fig. 8c). Here, blue contours indicate weaker snow, as seen at the interface between the old snow and storm snow, while red contours indicate stronger snow. The SI shown in Fig. 8e

indicates fragile snow at the end of the storm in a layer that starts at the new-snow/old-snow interface and goes up to 150 mm. This is further substantiated in the time to failure plot (Fig. 8f) that shows blue vertical lines indicating 1000 s to failure at 10:40 on 12 December 2020. From this analysis, we find that the SNOSS model with coefficients of strength from the Jamieson and Johnston (2001) accompanied with the densification model did predict the onset of natural avalanches. Despite this model's success, the ensemble of models (black line in Fig. 9b) predicted more stable conditions (minimum SI of 1.29). This result is indicative of a very sensitive snowpack and is further substantiated in the UAC

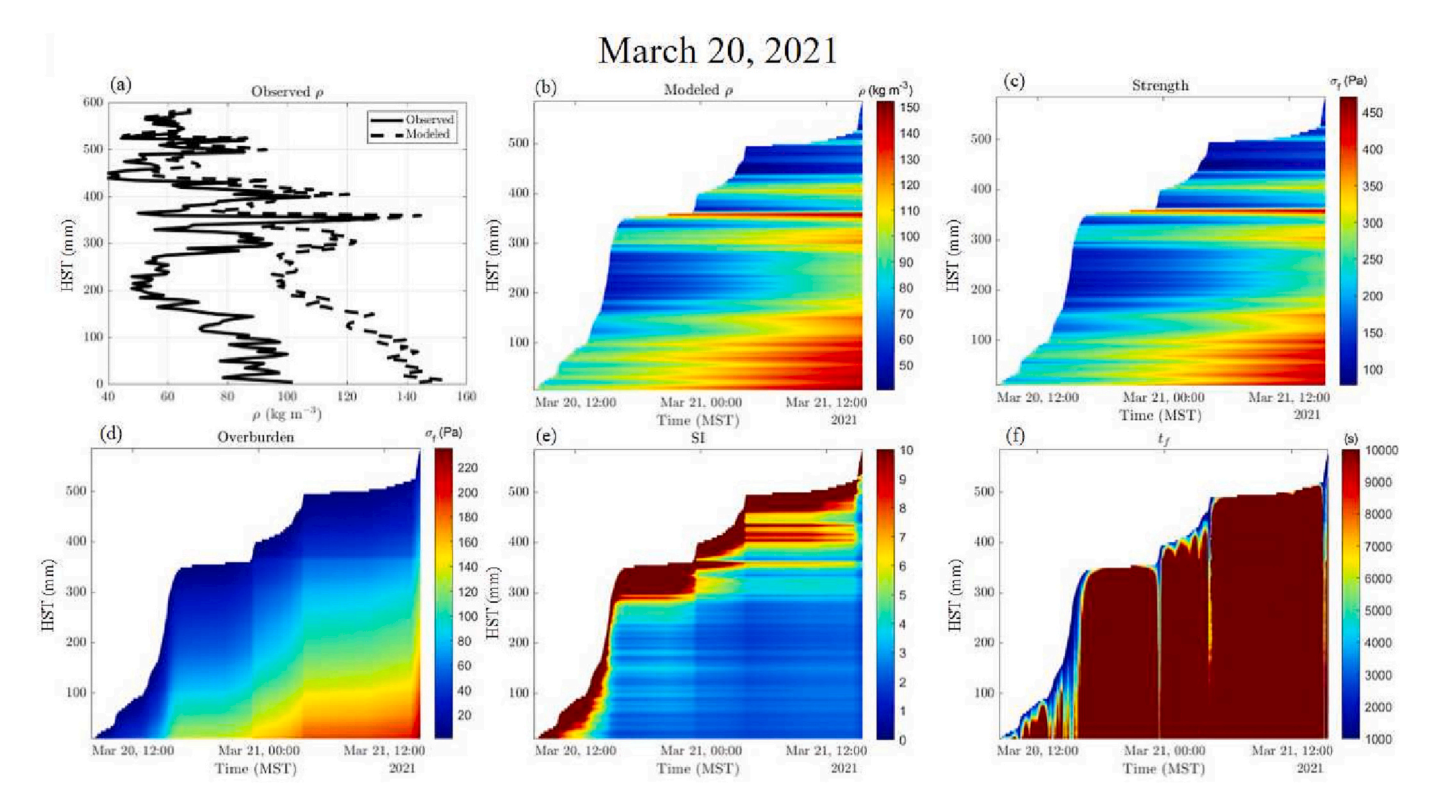


Fig. 12. Avalanche nowcasting plots produced with data from the DEID for storm beginning on 12 December 2020. (a) The measured and modeled density profile of the storm snow, (b) The modeled storm-snow density over the course of the storm, (c) the modeled shear strength of the storm snow, (d) the measured overburden force of the storm snow, (e) the stability index (ratio of subplot c to subplot d), and (f) the predicted time to failure in seconds of the storm snow.

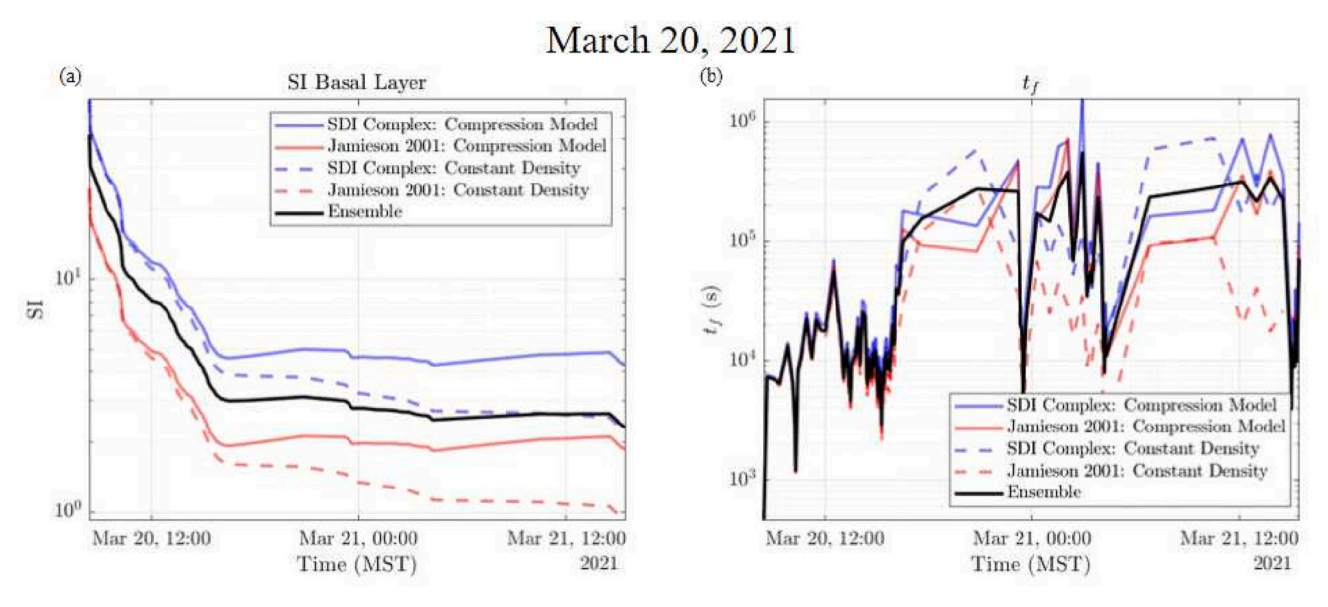


Fig. 13. Storm-snow/old-snow interface plots of (a) stability index (SI) and (b) the time to failure (t_f) for storm snow data beginning on 20 March 2021.

observational results shown in Table 3. A total five avalanches were reported with one natural, three user triggered, and one unknown trigger.

The 26 February 2021 storm produced a sensitive snowpack that led to five natural avalanches reported by the UAC and a natural avalanche observed with the infrasound (see Table 3). The initial density profile (Fig. 10a) from the storm does indicates a slight inversion, however, the low stability index near the surface is in part driven by the large overloading from the high precipitation rates observed over the course of the storm, tipping the scales toward instability. This can be observed in

Fig. 10f, which presents the time to failure model. Here, areas of red indicate strengthening, with vertical lines of light colour being associated with moments of high precipitation and increasing instability. These periods are identified at approximately 08:00 on 27 February 2021 and at noon on the same day. Both of these time periods correlated with a small natural avalanche cycle that was captured by the infrasound detection system (Table 3).

The last case study was 20 March 2021. During this storm, a total of 598 mm of snow consisting 33.4 mm of SWE fell at the site (Table 3). The snowpack density decreased in the lowest 200 mm above the storm-

snow/old-snow interface and then increased with a strong density inversion from 200 mm–350 mm as shown in Fig. 12a. According to the UAC observations (see Table 3), eight avalanches were reported that failed on the 200 mm–350 mm layer. Furthermore, the infrasound system indicated a natural avalanche at 07:35 on 21 February. Not only did the models capture this modest variation in SI within the storm snow, the SDI–Complexity model without densification and the Jamieson and Johnston (2001) model with densification both correctly predicted the onset of natural avalanches within the problematic layers (Figs. 12).

3.2. Tilt-board test results

DEID data from the 3 February 2021 storm is used to illustrate the ability of the DEID to identify weak layers both in terms of density and snowflake characteristics. As shown in Table 3, this storm lasted over two days producing 488 mm of snow and 31.8 mm of SWE. Furthermore, the maximum SWE rate observed by the DEID was nearly 29 mm/h. During a 12-h period on 5 February 2021 DEID data were captured and

compared to Alta Ski Patrol's manual observations and tilt-board tests. Fig. 14 presents a schematic of the tilt-board test results (a) along with profiles of the storm-snow density (b), SDI (c), Complexity (d), SWE rate (e), and modeled shear strength (f). Here, we use the SNOSS model with strength coefficients from the SDI-Complexity model without densification. This model was chosen since SDI and Complexity account for snowflake habit and therefore can be used to help interpret shear strength as a function of both density and crystal type. The horizontal red lines in Fig. 14 represent the weak layer/failure plane within the storm snow that failed during the tilt-board test.

For this test, 12-h of storm snow accumulated onto the board. During the test, the board was raised from the snow surface, tilted to 30° , and tapped following the procedure in Section 2.7. A shear failure occurred at a height of 152 mm from the board's surface after the fourth tap. To understand this result, we provide a detailed account of the variables measured by the DEID. Specifically, Fig. 14c shows a profile of SDI, which decreased throughout the storm cycle to its minimum at the weak layer snow height, from a value of ≈ 9 to 5, a reduction of 44%.

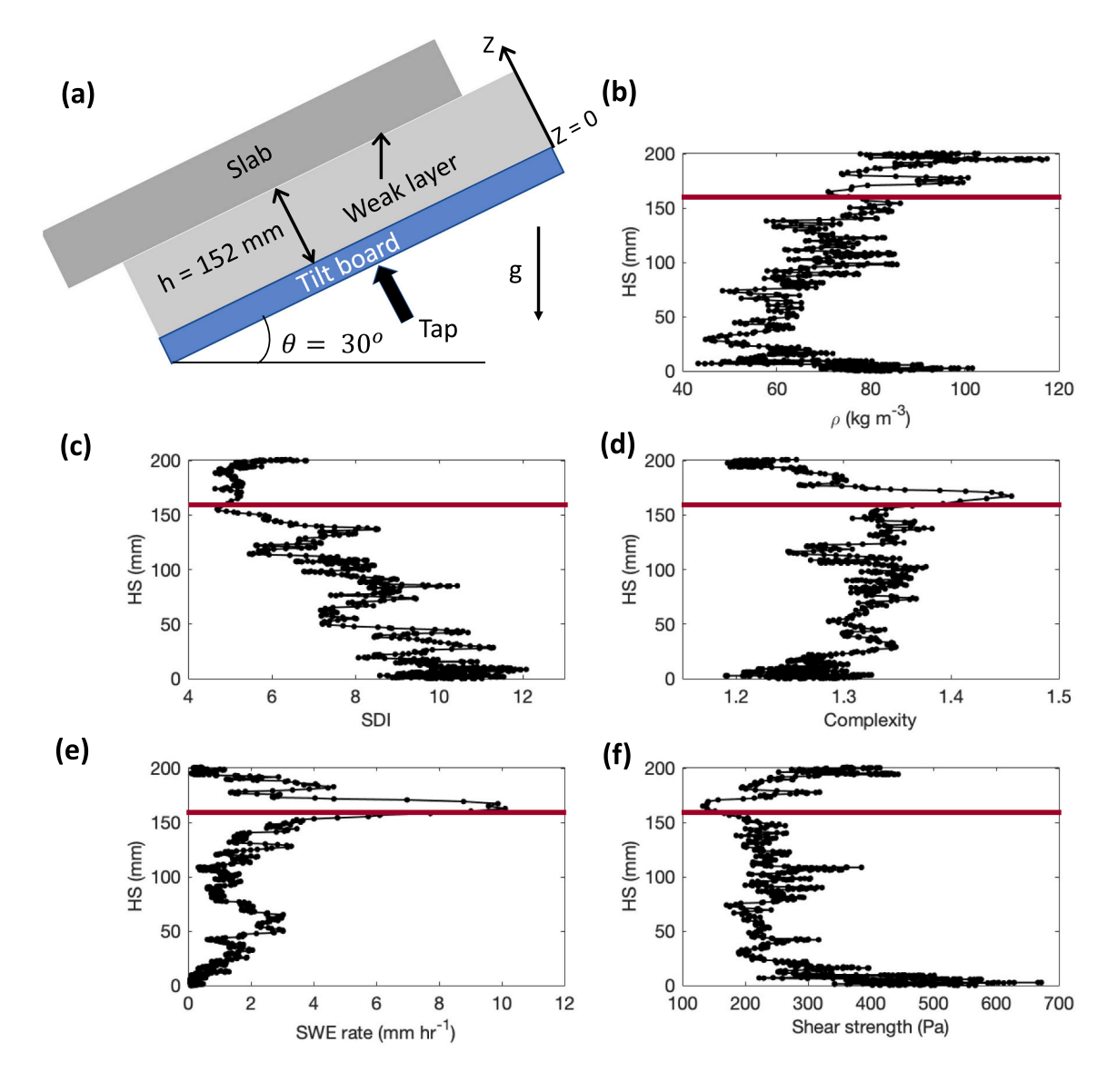


Fig. 14. 5-min averaged DEID data from a snow event on 5 Feb 2021 that correspond to a tilt-board test in which the snowpack failed at 152 mm from base (z = 0) in 4 taps (red, horizontal line). (a) Schematic of tilt-test set-up; (b) height of snow vs. density; (c) height of snow vs. SDI; (d) height of snow vs. Complexity; (e) height of snow vs. SWE rate (f) Height of snow vs. shear strength. (For interpretation of the references to colour in this figure legend, the reader is referred to the web version of this article.)

Meanwhile, Fig. 14d presents the snowflake Complexity, which increased from 1.3 to 1.5 at the shear layer (global maximum). From Eq. 7, we see that shear strength increases linearly with SDI, while Complexity acts as the exponent to the density ratio of snow to ice (since $\lambda = SDI$ and $\beta = Complexity$ for this model). Hence, the observed decrease in SDI and increase in Complexity led to weaker snow. Furthermore, from Section 2.4, the trend and combination of SDI and Complexity indicate that the snowflake habit migrated during this period from a columnar crystal to a planar-crystal habit. Finally, Fig. 14e shows that the SWE rate had a notable peak just above the height of the weak layer, indicating rapid development of overburden. The ρ , SDI and Complexity allows us to estimate the snow's shear strength and conclude that the layer located at 152 mm from the storm snow/old-snow interface is the weakest in the storm snow. A global minimum in shear strength is correctly modeled using DEID measurements inputs in agreement with results from the manually observed tilt-board test, in which a shear failure was observed at the same height, 152 mm. This result illustrates the power of the DEID to not only capture density profiles in great detail but to help determine storm-snow instabilities driven by variations in the habit of falling snowflakes.

4. Discussion

Within the SNOSS model, there is high sensitivity to the coefficients of strength, λ and β , used in Eq. 7 (see Fig. 5). Currently, strength coefficients are only defined for the predominate grain classification. For storm snow there is only one classification, precipitation particles. Here, we present and assess the SDI and Complexity parametrization for shear strength that accounts for grain habit, as shown in Section 2.4. While this shear-strength model requires further in-situ validation to relate SDI and Complexity to snowflake habit (Sec. 2.4) and snowflake habit to shear strength with shear frame tests, the method has begun to demonstrate here its ability to account for the varying strengths of different precipitation particles that owes to their structure.

It is known from expert experience that the type of snowflake habit influences shear-strength of the snowpack. Yet, currently, all stormsnow strength parametrizations (Fig. 5) assume the same shear-strength coefficient for precipitation particles and to behave solely as a function of snow density. The difficulty appears not to be a lack of awareness by practitioners but instead an inability to measure real-time snowflake type, and of measuring snow pack shear-strength immediately after a snowfall. Only the measured density of the layer is available as a diagnostic for determination of snowpack shear-strength (Eq. 7).

To assess the newly proposed SDI and Complexity shear strength parametrization in the context of the existing shear strength parametrizations, four strength formulations, as described in Section 2.2, as well as the ensemble of all members, are utilized to statistically predict the onset of storm snow avalanches. The four models and a summary of their performance are summarized in Table 4.

Of the four models, we found that the ensemble average of the members, Jamieson and Johnston (2001) with densification, and the SDI and Complexity model without densification provided the best

Table 4A summary of the shear-strength model evaluations. Jamieson 2001 is an abbreviation for Jamieson and Johnston (2001).

Model	Tendency	Explanation
Jamieson 2001, without densification model	Conservative	Lowest coefficients of strength, with constant density
Jamieson 2001, with densification model	Fair	Lowest coefficients of strength, with increasing density
SDI & Complexity, without densification model	Fair	Larger coefficients of strength, with constant density
SDI & Complexity, with densification model	Liberal	Larger coefficients of strength, with increasing density
Ensemble	Fair	Average of all models

predictions of the onset of natural avalanches. Although, as highlighted, the behavior of the stability index (SI) may vary across different regions or snow packs. By aggregating results from the SNOSS model and the natural avalanche activity, a specific SI may be used to further understand and refine each SI for a region of interest. For example, Jamieson 2001 without densification may predict a critical SI value of 0.5 whereas the SDI and Complexity model with densification may predict a critical SI of 3. The reason for the discrepancy may lie within the uncertainties in coefficients for the strength and the densification model parameters. With instruments such as the DEID, specific strength coefficients can be related to grain type and begin to narrow this uncertainty or refine the parametrizations. Furthermore, with the availability of more storms and DEID data, we can begin to validate Table 2. This validation would allow SI predictions and storm-snow avalanche forecasting solely with DEID data.

A critical point of difference among storm-snow stability models is the inclusion (or exclusion) of a density compression or densification model. The goal of any densification model is to account for compression the snowpack experiences due to metamorphic and vertical overburden stresses over the period of interest. In these models, snow is treated as a fluid that compresses based on the compactive viscosity of the snow. Initial observations from the SNOSS model outputs suggest that the results from the densification model compresses the snowpack more rapidly than anticipated. For example, on 2021 March 20 the snowpack at 200 mm was computed to increase from 45 kg m⁻³ to 110 kg m⁻³ in under 24 h, a 244% increase. We hypothesize that the reason for this observation is that the original densification model parameters, primarily the compactive viscosity, were determined "post-storm", rather than capture and applied during snowfall as performed here with the DEID. Traditional methods for capturing these parameters require digging snow pits, hours or even days after the storm snow has settled, compressed, and begun to undergo metamorphism. This gap in data collection from snowfall to observation impacts avalanche forecasting ability, as well as broader snowpack and hydrology models, which rely on densification models.

Moreover, the compactive viscosity is only a function of broad morphological classification and does not refine grain type for storm snow beyond the precipitation particle classification. Casson et al. (2008) performed a study to classify compactive viscosity as a function of precipitation type although no clear conclusions could be drawn. With the new high-resolution data from the DEID we anticipate being able to assess the compactive viscosity concurrent with an ongoing storm over short time scales of order of 1 h as well as for specific precipitation particle types. Identification of compactive viscosity terms as a function of crystal type at relevant storm timescales may enable improved storm-snow densification models for more accurate avalanche forecasting.

The SI, Eq. 11, represents the ratio of the shear strength of the storm snow to the overburden stress. Generally, when the SI value falls below unity, it is forecasted that the snowpack is unstable and natural avalanches may occur. Complicating factors in interpretation of SI computed at a single location for application to an entire region include terrain, spatial variability in snow accumulation, and differences in elevation and aspect. While the single location SNOSS assessment has these limitations, the results shown in Fig. 15 offer an initial look at the correlation between the minimum stability index (SI_{min}) calculated as the minimum SI over a storm from the ensemble averaged SI from the members in Table 1, and the number of reported natural and unknown triggered avalanches (Ax) observed in the Central Wasatch from the storm's start to three days post storm from the UAC observation database. The error bars in Fig. 15 present the standard deviation among the models. The corresponding SI_{min} versus Ax analysis provides greater context for interpreting the value of the SI as well as demonstrating the convergence or confidence of the SNOSS model's SI output. Initial findings suggest that, as anticipated, when SI_{min} decreases, there is increased instability and the number of avalanches observed increases.

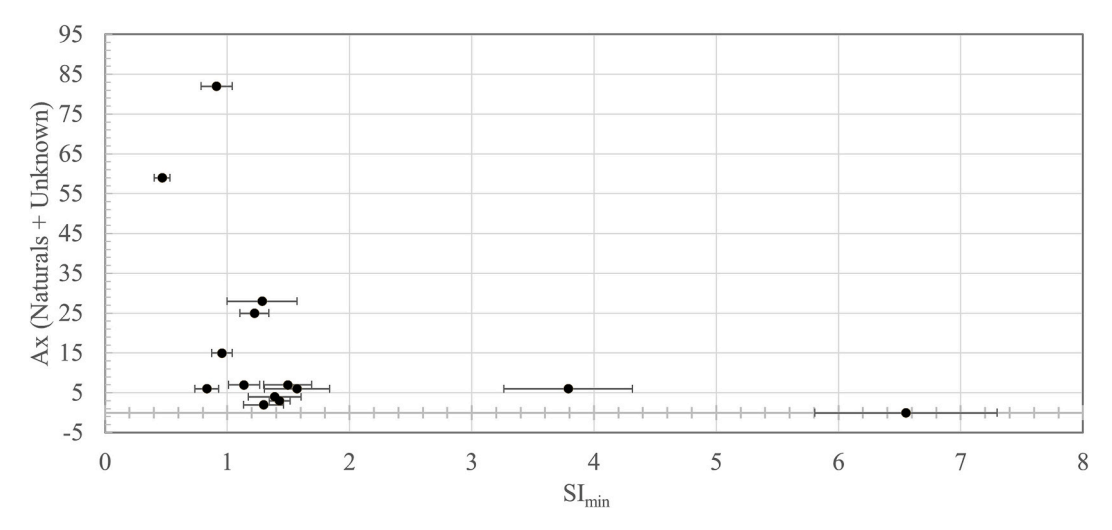


Fig. 15. The total number of natural and unknown triggered avalanches reported to the UAC from storm's end to three day post storm, compared to the ensemble averaged stability index. The error bars represent the standard deviation between the models for each case.

This relationship demonstrates the power the DEID and SNOSS model can employ for real time operational forecasting where storm snow avalanches are prevalent, an otherwise impossible task without real-time DEID data.

With more comprehensive measurements than presented here, it may become possible to make regional predictions of the number of avalanches using the SNOSS model. For example, in Fig. 15 reported widespread (>6 Ax) natural and unknown triggered avalanches began when the $\rm SI_{min}$ fell below a value of 1.5. Further studies designed relate the SNOSS model outputs to natural storm snow avalanches may be able to unlock more insight into the physical meaning of the spectrum of SI each model presents. We hypothesize that other data may be used to adapt this for applicability to regions outside of LCC, such as reactiveness of storm snow to explosive triggers, which is regularly documented by avalanche mitigation personal.

5. Conclusion

We have presented results that highlight the Differential Emissivity Imaging Disdrometer's potential for obtaining real-time measurements of critical variables required for prediction of snowpack instability and avalanche forecasting. Accurate measurements of precipitation intensity, snow density, and accumulation of snow and water are measured with the DEID in a particle-by-particle fashion. None of these measurements were previously available at such high resolution. These basic variables by themselves are valuable to avalanche forecasters who often use heuristics based on these variables (e.g., Perla, 1970) to provide warnings in their forecasts. However, despite the advancements in measurement techniques and in weather and avalanche forecasting, predicting the onset of storm-snow avalanches is still a complex issue. Works from Dkengne Sielenou et al. (2021); Pérez-Guillén et al. (2022) demonstrate the impact large data aggregation can have on region-wide avalanche forecasting, but the inherent local-scale temporal and spatial variability of avalanches will continue to be a challenge.

We have introduced two new parameters based on DEID measurements including the snow density index (SDI), which is the ratio of the actual projected snowflake area measured on the DEID's hotplate to the melted area of the snowflake, and the snowflake's Complexity, or the ratio of the area of the smallest ellipse altogether containing the particle cross-section to the actual cross-sectional area of the hydrometeor. Preliminary results indicate that classification of snowflake habit based on these parameters is possible using the DEID. Bair et al. (2012) noted that in half of all U.S. avalanche fatalities, the type failure crystal, or grain type at the bed surface of the avalanche, is not known because the

crystals can metamorphose in the snowpack and are difficult to measured during a storm. Continuous measurements from the DEID combined with simple shear-strength models provide stability indices of storm snow and time-to-failure metrics. These results highlight potential nowcasting products that a coupled DEID and SNOSS model can provide.

Following on the work presented here, future objectives include exploiting, for example, the DEID's ability to estimate the depth of shear layers within fresh storm snow and the overburden weight. These data could be combined with slide-path areas and elevation profiles to yield estimates of the potential destructive scale and energy of a storm-snow avalanche (Schleiss and Schleiss, 1970). The analysis could be performed for relevant slide paths of interest either in real time (nowcasting) or in a forecasting manner. In addition, we have found that the parameterization of the compactive viscosity in the SNOSS model may be too aggressive, leading to overly rapid densification and producing higher shear strengths within the modeled snowpack (Eq. 7). We hypothesize that improvements to the SNOSS model can be made by performing field and lab experiments to refine parameters related to grain structure. Furthermore, what remains poorly understood is how mixtures of different snow-grain types impact the strength of different layers. Currently, our SNOSS or stability-index model employs a linear average of SDI and Complexity for all types of snow crystals contained in a 5-mm layer, which then are used to compute the strength of the layer (α and β). It is not clear if this is the best way to aggregate snowflake habit to determine snow strength. Future work should investigate the relationship between snow-crystal type and shear strength using DEID differentiation of particle types and manual measurements of shear strength from shear frame tests.

In summary, we explored a simple and promising snow-stability index model that makes use of unique, highly detailed continuous measurements of key snowflake parameters using the Differential Emissivity Imaging Disdrometer. Future studies could include sophisticated, physics-based avalanche models such as SNOWPACK or CROCUS. Combining advanced avalanche modeling tools with the DEID diagnostics and Infrasound Detection Systems can be expected to provide the ingredients necessary to significantly advance the state of science for avalanche forecasting.

CRediT author statement

Travis Morrison: Writing, original draft, Software, Formal analysis; Trent Meisenheimer: Conceptualization, Methodology, Investigation, Writing, oringal draft; Spencer Donovan: Methodology, Investigation; Tim Garrett: Supervision, Conceptualization, reviewing and editing; Dhiraj Singh: Writing-reviewing and editing; Eric Pardyjak: Conceptualization, Methodology, Investigation, Writing-reviewing and editing.

Declaration of Competing Interest

The authors declare the following financial interests/personal relationships which may be considered as potential competing interests:

Travis Morrison reports a relationship with Particle Flux Analytics, Inc. that includes: employment. Travis Morrison reports a relationship with Alta Ski Area that includes: consulting or advisory. Travis Morrison reports a relationship with Utah Avalanche Center that includes: consulting or advisory. Timothy Garrett reports a relationship with Particle Flux Analytics, Inc. that includes: equity or stocks. Trent Meisenheimer reports a relationship with Utah Avalanche Center that includes: employment. Dhiraj Singh has patent Differential emissivity based evaporable particle measurement pending to Particle Flux Analytics, Inc. Timothy Garrett has patent Differential emissivity based evaporable particle measurement pending to Particle Flux Analytics, Inc. Eric Pardyjak has patent Differential emissivity based evaporable particle measurement pending to Particle Flux Analytics, Inc.

Data availability

Data will be made available on request.

Acknowledgments

We wish to thank the Transportation Avalanche Research Pool (TARP) and our department of transportation champions, Steven Clark and Jamie Yount, for their guidance and support during the project. We thank Allan Reaburn and his colleagues at Particle Flux Analytics for their key contributions in the development of DEID. We thank Dave Richards and the Alta Ski Patrol for their help and contributions, which were critical to facilitating the field validation study at Alta Ski Area. We thank the Utah Avalanche Center for providing access to archived backcountry observations and data. We are also thankful to Mark Saurer for the help working with UDOT infrasound data. We thank Karl Birkeland and Ethan Greene for their help in the proposal phase of the project. In addition to the support provided by TARP, this research was accomplished via support from the U.S. National Science Foundation grants number PDM-1841870 and AGS-2210179 awarded to the University of Utah and the United States Department of Energy, Office of Science, award number DE-SC 0017168, awarded to Particle Flux Analytics, Inc.

References

- American Avalanche Association, 2022. Snow, Weather, and Avalanches: Observational Guidelines for Avalanche Programs in the United States, 4rd ed. Denver, CO. Print.
- Bair, E.H., Simenhois, R., Birkeland, K., Dozier, J., 2012. A field study on failure of storm snow slab avalanches. Cold Reg. Sci. Technol. 79, 20–28. https://doi.org/10.1016/j. coldregions.2012.02.007.
- Bartelt, P., Lehning, M., 2002. A physical SNOWPACK model for the Swiss avalanche warning part I: numerical model. Cold Reg. Sci. Technol. 35, 123–145. https://doi. org/10.1017/s1350482704001355. snow Science.
- Brun, E., Rey, L., 1987. Field study on snow mechanical properties with special regard to liquid water content. IAHS Publ. 162, 183–193.
- CAIC, 2022. CAIC Statistics and Reporting. https://www.avalanche.state.co.us/accidents/statistics-and-reporting/. Accessed: 2022-06-27.
- Casson, J., Stoelinga, M., Locatelli, J., 2008. Evaluating the importance of crystal-type on new snow instability: a strength vs. stress approach using the snoss model. In: Proceedings of the 2008 International Snow Science Workshop, Whistler, BC, pp. 612-619.
- Conway, H., Wilbour, C., 1999. Evolution of snow slope stability during storms. Cold Reg. Sci. Technol. 30, 67–77.
- Dkengne Sielenou, P., Viallon-Galinier, L., Hagenmuller, P., Naveau, P., Morin, S., Dumont, M., Verfaillie, D., Eckert, N., 2021. Combining random forests and class-balancing to discriminate between three classes of avalanche activity in the french alps. Cold Reg. Sci. Technol. 187, 103276. https://www.sciencedirect.com/science/article/pii/S0165232X21000574. https://doi.org/10.1016/j.coldregions.2021.10 3276.

- Dunnavan, E.L., Jiang, Z., Harrington, J.Y., Verlinde, J., Fitch, K., Garrett, T.J., 2019. The shape and density evolution of snow aggregates. J. Atmos. Sci. 76, 3919–3940. https://doi.org/10.1175/JAS-D-19-0066.1.
- EAWS, 2022. EAWS Fatalities. https://www.avalanches.org/fatalities/. Accessed: 2022-06-27
- Fierz, C., Armstrong, R.L., Durand, Y., Etchevers, P., Greene, E., McClung, D.M., Nishimura, K., Satyawali, P.K., Sokratov, S.A., 2009. The International Classification for Seasonal Snow on the Ground.
- Fohn, P., 1966. The rutschblock as a practical tool for slope stability evaluation. IAHS Publ. 162, 223–228.
- Garrett, T.J., Fallgatter, C., Shkurko, K., Howlett, D., 2012. Fall speed measurement and high-resolution multi-angle photography of hydrometeors in free fall. Atmos. Meas. Tech. 5, 2625–2633. https://doi.org/10.5194/amt-5-2625-2012.
- Greene, E., Birkeland, K.W., Elder, K., Johnson, G., Landry, C., McCammon, I., Moore, M., Sharaf, D., Sterbenz, C., Tremper, B., et al., 2004. Snow, Weather, and Avalanches: Observational Guidelines for Avalanche Programs in the United States. American Avalanche Association, Pagosa Springs, Colorado, p. 150.
- Havens, S., Marshall, H., Covington, C., Nicholson, B., Conway, H., 2012. Real Time Snow Slope Stability Modeling of Direct Action Avalanches, in: Proceedings of the 2012 International Snow Science Workshop. Anchorage, Alaska, pp. 866–871.
- Hayes, P., Wilbour, C., Gibson, R., Marshall, H., Conway, H., 2004. A simple model of snow slope stability during storms. In: Proceedings of the 2004 International Snow Science Workshop, Jackson Hole, WY, pp. 165–171.
- Jamieson, J.B., . Avalanche prediction for persistent snow slabs. URL: https://prism.uc algary.ca/handle/1880/29827 https://doi.org/10.11575/PRISM/10182.
- Jamieson, J., Johnston, C., 1998. Refinements to the stability index for skier-triggered dry-slab avalanches. Ann. Glaciol. 26, 296–302.
- Jamieson, J.B., Johnston, C.D., 2001. Evaluation of the shear frame test for weak snowpack layers. Ann. Glaciol. 32, 59–69. https://doi.org/10.3189/ 172756401781819472.
- Jóhannesson, T., Porsteinn, A., 1992. Accidents and economic damage due to snow avalanches and landslides in Iceland. Jökull 81–94.
- Kojima, K., 1967. Densification of Seasonal Snow Cover. In: Physics of Ice and Snow: Proceed. Int. Conf. on Low Temperature Science. Institute of Low Temperature Science, Sapporo, Japan, pp. 929–952.
- Mayer, S., van Herwijnen, A., Ulivieri, G., Schweizer, J., 2020. Evaluating the performance of an operational infrasound avalanche detection system at three locations in the swiss alps during two winter seasons. Cold Reg. Sci. Technol. 173, 102962. URL: https://www.sciencedirect.com/science/article/pii/S0165232 X19302332 https://doi.org/10.1016/j.coldregions.2019.102962.
- McClung, D., Schaerer, P.A., 2006. The Avalanche Handbook, 3rd ed. Mountaineers Books. Seattle. WA.
- Morin, S., Horton, S., Techel, F., Bavay, M., Coléou, C., Fierz, C., Gobiet, A., Hagenmuller, P., Lafaysse, M., Ližar, M., Mitterer, C., Monti, F., Müller, K., Olefs, M., Snook, J.S., van Herwijnen, A., Vionnet, V., 2020. Application of physical snowpack models in support of operational avalanche hazard forecasting: a status report on current implementations and prospects for the future. Cold Reg. Sci. Technol. 170, 102910. https://doi.org/10.1016/j.coldregions.2019.102910.
- Nalli, W., 2019. Personal Communication.
- Pérez-Guillén, C., Techel, F., Hendrick, M., Volpi, M., van Herwijnen, A., Olevski, T., Obozinski, G., Pérez-Cruz, F., Schweizer, J., 2022. Data-driven automated predictions of the avalanche danger level for dry-snow conditions in Switzerland. Nat. Hazards Earth Syst. Sci. 22, 2031–2056. URL: https://nhess.copernicus.org/articles/22/2031/2022/ https://doi.org/10.5194/nhess-22-2031-2022.
- Perla, R.I., 1970. On contributory factors in avalanche hazard evaluation. Can. Geotech. J. 7, 414–419.
- Perla, R., Beck, T.M.H., Cheng, T.T., 1982. The shear strength index of alpine snow. Cold Reg. Sci. Technol. 6, 11–20. https://doi.org/10.1016/0165-232x(82)90040-4.
- Praz, C., Roulet, Y.A., Berne, A., 2017. Solid hydrometeor classification and riming degree estimation from pictures collected with a multi-angle snowflake camera. Atmos. Meas. Tech. 10, 1335–1357.
- Rees, K.N., Singh, D.K., Pardyjak, E.R., Garrett, T.J., 2021. Mass and density of individual frozen hydrometeors. Atmos. Chem. Phys. 21, 14235–14250.
- Roch, A., 1966. Les déclenchements d'avalanche. IAHS Publ. 69, 86–99.
- Schleiss, V., Schleiss, W., 1970. Avalanche hazard evaluation and forecast, roger pass, glacier national park. in ice engineering and avalanche forecasting and control. In: Technical Memorandum 98. Natl. Res. Counc. Can, pp. 115–122.
- Schweizer, J., Jamieson, J.B., Skjonsberg, D., 1998. Avalanche forecasting for transportation corridor and backcountry in glacier national park (bc, canada). Proc. Anniv. Conf. 238–244.
- Schweizer, J., Bellaire, S., Fierz, C., Lehning, M., Pielmeier, C., 2006. Evaluating and improving the stability predictions of the snow cover model snowpack. Cold Reg. Sci. Technol. 46, 52–59.
- Singh, D.K., Donovan, S., Pardyjak, E.R., Garrett, T.J., 2021. A differential emissivity imaging technique for measuring hydrometeor mass and type. Atmospheric. Meas. Tech. 14, 6973–6990. URL: https://amt.copernicus.org/articles/14/6973/2021/ https://doi.org/10.5194/amt-14-6973-2021.
- Singh, D.K., Pardyjak, E.R., Garrett, T.J., 2023. Time-Resolved Snow Density Measurements Using a Differential Emissivity Imaging Disdrometer. Atmospheric Measurement Techniques. Under preparation.
- Smith, C.D., Kontu, A., Laffin, R., Pomeroy, J.W., 2016. An assessment of two automated snow water equivalent instruments during the WMO Solid Precipitation Intercomparison Experiment. Cryosphere 11, 101–116. URL: https://tc.copernicus. org/articles/11/101/2017/ https://doi.org/10.5194/tc-11-101-2017.
- Vionnet, V., Brun, E., Morin, S., Boone, A., Faroux, S., Moigne, P.L., Martin, E., Willemet, J.M., 2012. The detailed snowpack scheme Crocus and its implementation

in SURFEX v7.2. Geosci. Model Dev. 5, 773–791. https://doi.org/10.5194/gmd-5-773-2013

Voight, B., Coauthors, 1990. Snow avalanche hazards and mitigation in the united states. https://doi.org/10.17226/1571. Vyas, M., 2009. Infrasound avalanche monitoring system research evaluation. Utah Department of Transportation.